Physics of Fluids

Distributed surface compliance for airfoil tonal noise reduction at various loading conditions

Cite as: Phys. Fluids **34**, 046113 (2022); https://doi.org/10.1063/5.0087350
Submitted: 04 February 2022 • Accepted: 26 March 2022 • Published Online: 19 April 2022

Irsalan Arif, Garret C. Y. Lam, Randolph C. K. Leung, et al.

AIP Publishing

Physics of Fluids ARTICLE scitation.org/journal/phf

Distributed surface compliance for airfoil tonal noise reduction at various loading conditions

Cite as: Phys. Fluids **34**, 046113 (2022); doi: 10.1063/5.0087350
Submitted: 4 February 2022 · Accepted: 26 March 2022 ·
Published Online: 19 April 2022

Irsalan Arif, Garret C. Y. Lam, Randolph C. K. Leung,[a] and Muhammad Rehan Naseer

AFFILIATIONS

Department of Mechanical Engineering, The Hong Kong Polytechnic University, Hong Kong, People's Republic of China

[a] Author to whom correspondence should be addressed: mmrleung@polyu.edu.hk

ABSTRACT

A novel concept of utilizing distributed surface compliance to achieve airfoil tonal noise reduction at various loading conditions is proposed. The aeroacoustics of airfoil configuration subjected to different loading conditions at angles of attack (AoAs) from 3° to 7° are numerically studied using high-fidelity two-dimensional direct aeroacoustic simulation at Reynolds and Mach numbers of 5×10^4 and 0.4, respectively. Initially, airfoil configurations mounted with single elastic panel (SEP) at individual AoA are designed with the knowledge of respective rigid airfoil flow characteristics. Stemming from the analysis of noise reduction potential of SEP configurations using a reduced-order modeling approach, a distributed surface compliance (DSC) airfoil configuration utilizing three resonating panels is designed to attain airfoil tonal noise reduction over entire range of AoA. Comprehensive acoustic analyses establish that the DSC airfoil could provide a maximum noise reduction ranging from 3 to 7 dB without any sacrifice in airfoil aerodynamics. The extent of noise reduction with DSC airfoil is found dependent on the flow-induced modal responses of the panels. At lower AoA, the panel(s) resonate in their designed structural modes, which remarkably weaken the flow instabilities convecting over the airfoil suction surface and eventually airfoil noise radiation. At higher AoA, the panel responses deviate from their designed structural mode shapes but could still give less noise reduction. Therefore, the designed DSC airfoil shows a feasible concept for tonal noise reduction over a wide range of operational AoA, which substantiates its applicability for aerodynamic devices at low Reynolds numbers.

I. INTRODUCTION

Airfoil trailing edge noise is one of the most critical aspect associated with its operations. The trailing edge noise generated by the airfoil at high Reynolds number (*Re*) is generally broadband in nature;[1] whereas, at low *Re,* the airfoil self-noise is dominated by distinct high amplitude tones.[2–5] Owing to substantial increase in the utilization of low *Re* aerodynamic devices including wind turbines, cooling fans, unmanned air vehicles, gliders, and commercial drones over the last few years, the issue of undesirable noise generation has significantly restricted the application of these devices to their full potential. The mechanism of airfoil tonal noise generation has been widely investigated over the years in a number of studies.[2,6–10] At low *Re*, the boundary layer over the airfoil surface is laminar but potentially unstable. Under these conditions, the hydrodynamic instabilities, such as Tollmien–Schlichting (T–S) waves, convect downstream and grow until it reaches the airfoil trailing edge and roll up into vortices.[4,11–13] The generated vortices subsequently interact with the trailing edge and generate a scattered oscillating pressure field with a similar frequency to that of T–S waves. This oscillating field moves upstream and provides an acoustic feedback mechanism.[4,7,14,15]

Although the mechanism of airfoil tonal noise has been well studied and understood, only a few studies are devoted to modify it for noise reduction. The existing approaches are mostly limited to modifications of trailing and leading edges modifications such as serrations, porosity, etc.[16–22] However, the effectiveness of these approaches is restricted to a certain flow condition or at a specific airfoil loading condition, which limits their application in the real-world environment. Chong and Joseph[23] investigated the effectiveness of NACA 0012 airfoil with serrated trailing edges in tonal noise reduction at low *Re* for a fixed angle of attack (AoA) of 4.2°. The geometric parameters including serration angle and serrations height were found to be major contributing factors in tonal noise reduction, which significantly weakened the normal velocity fluctuations within the small region of wake from the laminar boundary layer. The utilization of tubercles has shown favorable flow characteristics for tonal noise reduction by reducing the coherence of the wake.[24–26] Hansen *et al.*[27] claimed in their experimental and numerical investigations that the streamwise vortices generated by the tubercles and the variation in separation bubble lead to significant tonal noise reduction. These characteristics of the tubercles alter the flow instabilities in the shear layer and affect the coherence of the vortex shedding in the airfoil wake, which results in a reduction in trailing edge noise at specific flow conditions. Moreau and Doolan[28] employed different sawtooth trailing edge serrations on a flat plate and experimentally investigated their tonal noise reduction at two different *Re*. Their investigation revealed a significant noise reduction by wide serrations, which were responsible for reduction in the magnitude of velocity fluctuations at low frequencies. Recently, Jiang *et al.*[29] experimentally tested a series of trailing edge treatments of the NACA 0012 airfoil such as porous edges, poro-serrated edges, and curved serrated porous edges at low to moderate *Re* for a fixed AoA of 4°. Their investigation revealed that a combination of porous and serrated geometries resulted in a noise reduction up to 14.2 dB.

In recent years, flow and noise control utilizing structural elasticity has also been attempted on the airfoil.[30–33] Talboys *et al.*[34] observed that flaplets installed on NACA0012 airfoil are able to stabilize the shear layer at low *Re* and low AoA, which could lead to thinning of the boundary layer on the airfoil suction surface. Schlanderer and Sandberg[35] numerically investigated a flat plate with a flexible trailing edge and achieved some noise suppression at low to moderate frequencies as compared with a flat plate with a rigid trailing edge; however, an increase in noise level was observed at some eigen-frequencies of flexible trailing edge. Recently, Arif *et al.*[36] utilized the structural resonance of a short elastic panel on an airfoil surface for tonal noise reduction at low *Re* and AoA of 5°.

Although the aforementioned noise control methods have achieved some tonal noise reduction, their design and effectiveness are mostly evaluated and restricted to specific/fixed flow conditions only. Nowadays, many modern low *Re* aerodynamic devices are required to operate at variable loading conditions such as wind turbines operating under high wind sheared flows, unmanned air vehicles under search and rescue operations, etc. It is well known that the changes in flow conditions, for example AoA, directly affect the boundary layer characteristics over the airfoil such as flow separation/reattachment points, natural growth of the boundary layer instabilities, and length of laminar separation bubble (LSB).[37–42] As such, it is not surprising to conceive that most of the aforementioned modifications for noise reduction may not remain as effective as in the specific flow conditions the noise reduction method is devised.

Motivated by the interest in overcoming the said noise control challenge, a novel concept of a distributed surface compliance (DSC) airfoil is proposed in this study, which could provide tonal noise reduction at various loading conditions. The local surface compliance is provided by a short elastic panel mounted on the airfoil surface. The design methodology of DSC airfoil consists of three major stages. In the initial stage, flow characteristics over the rigid surface (RS) airfoil are analyzed at different AoAs. Subsequently, airfoil configurations with single elastic panel are designed and their effectiveness is evaluated at different AoAs by a reduced order model, named as perturbation evolution method (PEM) developed by the authors.[43] Finally, a DSC airfoil with multiple panels is designed and its effectiveness in tonal noise reduction at different loading conditions by means of varying the AoA is evaluated using high-fidelity direct aeroacoustic simulation (DAS).

This paper is organized as follows. Section II describes the formulation of the problem and the numerical methodology adopted in the present study. The analysis of RS airfoil is carried out in Sec. III, which is followed by the design and evaluation of airfoil configurations with single elastic panel in Sec. IV. Finally, the design concept and a comprehensive aeroacoustics analysis of DSC airfoil is presented in Sec. V.

II. PROBLEM FORMULATION AND NUMERICAL METHODS

The present problem of interest involves complex interactions between unsteady flow, panel structural vibration, and acoustics. Hence, a numerical approach capable of resolving all these physical phenomena covering both aerodynamic and acoustic scales is required. Therefore, we adopt the DAS approach for its capability of resolving the inherent coupling between the unsteady airfoil aerodynamic and acoustic solutions with sufficient accuracy. The governing equations for aeroacoustical flow and structural solvers and their implementation strategy are briefly discussed in the following sections.

A. Aeroacoustical flow solver

The aeroacoustic problem in the present study is modeled by compressible Navier–Stokes (N–S) equations and the equation of state, which govern all the physical aspects of flow dynamics and acoustics. To solve the unsteady N–S equations, conservation element and solution element (CE/SE) method is adopted. It is a robust and highly accurate method, which enforces strict physical conservation laws in N–S equations in both space and time domains.[44] Unlike other conventional numerical schemes that are based on finite difference and finite volume methods, it unifies the treatment of both space and time domains. Details of its implementation are discussed in Lam *et al.*,[44,45] which show success of using the CE/SE method to analyze the complex aeroacoustic interactions at both subsonic and supersonic flow speeds within the duct. Recently, Lam and Leung[46] and Arif *et al.*[47] have also utilized the CE/SE method to accurately capture the aeroacoustic phenomenon of airfoil flow and the acoustic feedback mechanism responsible for the airfoil tonal noise generation.

Unless otherwise specified, all the variables in the present study are considered in their non-dimensional form. The dimensional quantities are denoted with the hat symbol (ˆ) and those without are their normalized counterparts. Taking the fluid properties of freestream with dimensional velocity $\hat{U}_\infty$ and airfoil chord $\hat{c}$ as reference, the two-dimensional N–S equations in strong conservative form can be written as

$$\frac{\partial \boldsymbol{U}}{\partial t} + \frac{\partial(\boldsymbol{F} - \boldsymbol{F}_v)}{\partial x} + \frac{\partial(\boldsymbol{G} - \boldsymbol{G}_v)}{\partial y} = 0, \tag{1}$$

where the flow flux conservation variables are defined by

$$\begin{aligned}
\boldsymbol{U} &= [\rho \quad \rho u \quad \rho v \quad \rho E]^T,\\
\boldsymbol{F} &= \left[\,\rho\, u \quad \rho\, u^2 + p \quad \rho\, uv \quad (\rho E + p)u\right]^T,\\
\boldsymbol{F}_v &= (1/Re)[0 \quad \tau_{xx} \quad \tau_{xy} \quad \tau_{xx}u + \tau_{xy}v - q_x]^T,\\
\boldsymbol{G} &= \left[\rho v \quad \rho uv \quad \rho v^2 + p \quad (\rho E + p)v\right]^T,\\
\boldsymbol{G}_v &= (1/Re)[0 \quad \tau_{xy} \quad \tau_{yy} \quad \tau_{xy}u + \tau_{yy}v - q_y]^T.
\end{aligned}$$

The normal and shear stresses are defined as

$$\tau_{xx} = (2/3)\mu(2\partial u/\partial x - \partial v/\partial y),$$
$$\tau_{xy} = \mu(2\partial u/\partial y - \partial v/\partial x),$$
$$\tau_{yy} = (2/3)\mu(2\partial v/\partial y - \partial u/\partial x).$$

The heat flux components are defined as

$$q_x = \left[\mu/(\gamma - 1)PrM^2\right](\partial \mathrm{T}/\partial x),$$
$$q_y = \left[\mu/(\gamma - 1)PrM^2\right](\partial \mathrm{T}/\partial y).$$

The Reynolds number, Mach number, and Prandtl Number can be calculated by

$$Re = \hat{\rho}_\infty \hat{U}_\infty \hat{c}/\hat{\mu}_\infty, \quad M = \hat{U}_\infty/\hat{a}_\infty, \quad Pr = \hat{c}_{p,\infty}\hat{\mu}_\infty/\hat{k}_\infty = 0.71,$$

where, the specific heat ratio $\gamma = 1.4$, $\hat{c}_{p,\infty}$ is the specific heat at constant pressure and $\hat{k}_\infty$ is the thermal conductivity. The total energy and pressure are calculated by

$$E = p/\rho(\gamma - 1) + (u^2 + v^2)/2, p = \rho \mathrm{T}/\gamma M^2,$$

The non-dimensional time and frequency are defined by

$$t = \hat{t}\hat{U}_\infty/\hat{c}, \quad f = \hat{f}\hat{c}/\hat{U}_\infty.$$

B. Structural solver and aeroacoustic-structural coupling

The nonlinear dynamic response of the elastic panel is modeled by solving the one-dimensional plate equation to the simplest approximation.[48] The normalized governing equation for panel displacement can be written as

$$S_{\mathrm{EP}}\frac{\partial^4 w}{\partial x^4} - (T_{\mathrm{EP}} + N_{\mathrm{EP}})\frac{\partial^2 w}{\partial x^2} + \rho_{\mathrm{EP}} h_{\mathrm{EP}}\frac{\partial^2 w}{\partial t^2} + C_{\mathrm{EP}}\frac{\partial w}{\partial t} + K_{\mathrm{EP}} w = p_{ex}, \tag{2}$$

where w is the panel displacement from its undisturbed position, $S_{\mathrm{EP}} = \hat{S}_{\mathrm{EP}}/\hat{\rho}_\infty \hat{U}_\infty^2 \hat{c}^3$ is the panel bending stiffness, $E_{\mathrm{EP}} = \hat{E}_{\mathrm{EP}}\hat{U}_\infty^2 / \hat{\rho}_\infty \hat{c}^4$ is the Young's Modulus of panel, ν is the Poisson's ratio, $T_{\mathrm{EP}} = \hat{T}_{\mathrm{EP}} / \hat{\rho}_\infty \hat{U}_\infty^2 \hat{c}$ is the external tensile stress in tangential direction, $N_{\mathrm{EP}} = (E_{\mathrm{EP}} h_{\mathrm{EP}}/2L_{\mathrm{EP}}) \int_0^{L_{\mathrm{EP}}} (\partial w/\partial x)^2 dx$ is the internal tensile stress in the tangential direction, $C_{\mathrm{EP}} = \hat{C}_{\mathrm{EP}}/\hat{\rho}_\infty \hat{U}_\infty$ is the structural damping coefficient of panel, $K_{\mathrm{EP}} = \hat{K}_{\mathrm{EP}}\hat{c} / \hat{\rho}_\infty \hat{U}_\infty$ is the stiffness of the foundation supporting the panel and $p_{ex} = \hat{p}_{ex} / \hat{\rho}_\infty \hat{U}_\infty^2$ is the net pressure exerted on the panel surface. Stainless steel is assumed for panel material properties in this study. We consider a very thin elastic panel, which behaves similar to a membrane; therefore, C_{EP}, S_{EP}, and K_{EP} are taken as effectively zero.[48,49] Equation (2) is solved by the standard finite difference method. The nonlinear coupling between aeroacoustic fluctuation and panel structural dynamics is resolved with a monolithic scheme developed by Fan *et al.*[49] In essence, the scheme treats the fluid/panel system as a single entity and includes the effects of panel dynamics on aeroacoustical flow in an extra source term in the CE/SE governing equations [Eq. (1)], which is then solved with a Newton iteration method for its much faster convergence than conventional partitioned approach. The coupling scheme is fully validated with a series of benchmark aeroacoustic-structural interaction problems and is proven to accurately resolve aeroacoustic-structural coupling of increasing complexity.[49,50]

C. Reduced order modeling

It is widely acknowledged that DAS provides accurate insight of airfoil aeroacoustics, but it requires a significant amount of computational resources to complete a calculation. Using DAS for the design of an airfoil configuration based on multiple panels with unique structural properties and evaluation of its effectiveness in noise reduction for each iteration is not practically feasible. Therefore, a reduced-order modeling approach, namely perturbation evolution method (PEM),[43] is employed in the initial stage for the design and analysis of various single panel configurations to ascertain their noise suppression potential.

PEM is based on the analysis of evolution of weak perturbation, which is initiated with the information available from DAS solution of the RS airfoil. It is proven to be an effective tool[36] as it only requires 10% of the computational time required for a full DAS calculation. The effectiveness and accuracy of PEM have been successfully validated in Arif *et al.*[43] Only a brief overview of its adaptation is provided here. The normalized compressible N–S equations in two-dimensional form with a constant forcing term $\boldsymbol{S}$ may be written in a strong conservative form as

$$\frac{\partial \boldsymbol{U}}{\partial t} + \frac{\partial \boldsymbol{F}}{\partial x} + \frac{\partial \boldsymbol{G}}{\partial y} = \boldsymbol{S}. \tag{3}$$

We may express the unsteady flow in terms of a steady base flow and an infinitesimal perturbation [i.e., $\boldsymbol{U}(x, y, t) = \boldsymbol{U}_{base}(x, y) + \boldsymbol{U}'(x, y, t)$] and take the forcing term derived from spatial gradients of the base flow, so Eq. (3) becomes

$$\frac{\partial(\boldsymbol{U}_{base} + \boldsymbol{U}')}{\partial t} + \left(\frac{\partial \boldsymbol{F}}{\partial x} + \frac{\partial \boldsymbol{G}}{\partial y}\right)_{base} + \left(\frac{\partial \boldsymbol{F}}{\partial x} + \frac{\partial \boldsymbol{G}}{\partial y}\right)' = \boldsymbol{S} = \left(\frac{\partial \boldsymbol{F}}{\partial x} + \frac{\partial \boldsymbol{G}}{\partial y}\right)_{base}, \tag{4}$$

$$\Rightarrow \frac{\partial(\boldsymbol{U}_{base} + \boldsymbol{U}')}{\partial t} + \left(\frac{\partial \boldsymbol{F}}{\partial x} + \frac{\partial \boldsymbol{G}}{\partial y}\right)' = \frac{\partial \boldsymbol{U}'}{\partial t} + \left(\frac{\partial \boldsymbol{F}}{\partial x} + \frac{\partial \boldsymbol{G}}{\partial y}\right)' = 0, \tag{5}$$

as $\partial \boldsymbol{U}_{base}/\partial t = 0$. Note that the homogeneous Eq. (5) has the same mathematical form as the full nonlinear N–S equations [Eq. (1)], but all the primitive variables are replaced by their perturbations in the flux variables $\boldsymbol{U}$, $\boldsymbol{F}$, and $\boldsymbol{G}$.

For the present study, a broadband acoustic excitation is introduced, which can effectively produce weak perturbations within the flow continuously, which generates the hydrodynamic instabilities within the airfoil boundary layer.[14] The acoustic excitation function is defined as $p'_{inc} = p_A \sum_{n=1}^{100} \sin(2\pi t f_{exc,n} + \phi_n)$, where p_A is constant pressure amplitude, excitation frequencies $0.1 \le f_{exc,n} \le 10$ with a uniform increment of $\Delta f_{exc,n} = 0.1$ and uniformly random phase ϕ_n. A weak excitation of $p_A = 10^{-5}$ is introduced near the leading edge of airfoil at a location $(x, y) = (-0.015 \text{ and } -0.01)$. When the acoustic excitation interacts with the leading edge of airfoil, a downstream traveling wavepacket over the airfoil suction surface is generated, which

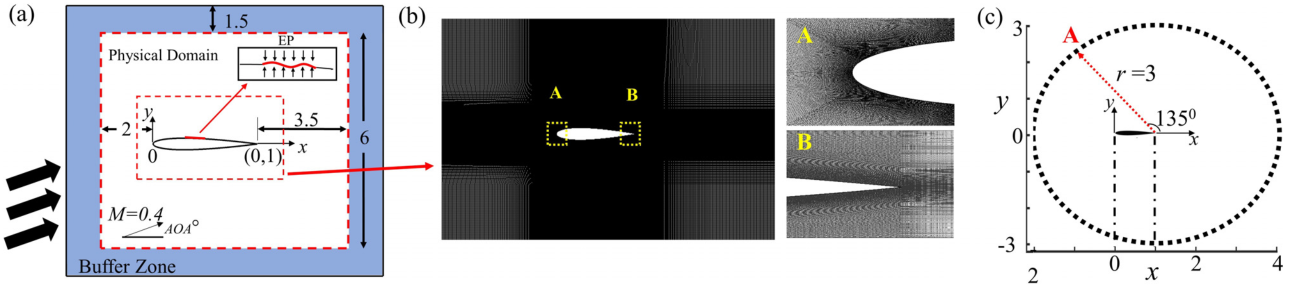

FIG. 1. (a) Schematic of computational domain; (b) mesh design with closeup views of airfoil leading and trailing edges; and (c) distribution of virtual probes around the airfoil.

excites a number of panel natural modal frequencies. Flow-induced structural resonance is likely to occur at the dominant frequency of naturally evolving airfoil boundary layer disturbance, and the panel would respond effectively in suppressing the flow instabilities in this condition.[43]

D. Numerical setup

A schematic sketch of the computational domain for the present study is shown in Fig. 1(a). The dimensions shown are all made dimensionless with airfoil chord chosen as the reference length (i.e., $\hat{L}_0 = \hat{c}$). A NACA 0012 airfoil with a sharp trailing edge is considered due to its popularity in low *Re* applications and the high availability of its aerodynamic and acoustic data in literature.[4,14,40,51] The airfoil is immersed in a freestream with $M = 0.4$ and $Re = 5 \times 10^4$, which enters the domain from left and bottom inlet boundaries of the domain. For the cases with elastic panels, the panel is flush-mounted on the suction surface of the airfoil with its both edges fixed. The NACA 0012 is modeled with its leading edge at $(x, y) = (0, 0)$. In order to avoid any erroneous acoustic reflection, a buffer zone with an exponentially stretched mesh of width 1.5 is set up around the physical domain. All domain boundaries adopt nonreflecting boundary condition[44] except the left and bottom boundaries, which are defined by inlet boundary condition. All solid surfaces including the elastic panel are prescribed with no-slip boundary condition.

The computational mesh is generated by structured quadrangular elements throughout the domain. In the application of CE/SE method, a quadrangle mesh element is split into four triangles using diagonal cross division.[44] In order to limit the computational cost, the mesh size around the critical locations including airfoil leading edge, trailing edge, and near wake [Fig. 1(b)] are given special considerations for guaranteeing sufficient resolution for resolving the boundary layer evolution and subsequent acoustic propagation. The wall normal resolution of the first grid point in the vicinity of airfoil leading and trailing edges is set to $\Delta y = 0.0005$ with a stretching ratio of 1.05% within the boundary layer. A comprehensive grid independence study has been carried out and already presented in Arif *et al.*[47] A grid with a total mesh size of 6.52×10^6 is chosen in the present study for its best compromise between accuracy and optimum requirement of computational resources. Details of the selected mesh sizes for the complete domain are listed in Table I.

For DAS calculations, the computational domain, grid size, and time step for the case of AoA = 3° and 5° are kept same. However, for AoA = 7°, the grid size near the airfoil surface is further refined by a factor of 2 so as to capture stronger flow unsteadiness within the boundary layer over the airfoil surface.[38] The time step size is also reduced accordingly for AoA = 7° to maintain the same CFL condition. For all calculations, the solution is sufficiently progressed until a time stationary state has been achieved. The solution is then further proceeded for a time episode equal to 40 flow convective passes for aerodynamic and acoustic analyses. The calculations are carried out in a parallel computing facility with 494 CPU cores for a total of approximately 94 000 CPU hours for each case. To analyze the acoustical characteristics, 180 virtual probes are placed all around the airfoil with azimuthal increment $d\theta = 2°$ at a radius $r = 3$ [Fig. 1(c)]. Furthermore, a total of 4000 virtual probes are placed within the boundary layer along suction and pressure surfaces of the airfoil to analyze the flow aerodynamic behavior.

E. Validation of numerical scheme

The validation of numerical setup is carried out by analyzing the flow characteristics over the airfoil and comparing them with literature.[3,39,52] Figure 2(a) shows the time-averaged friction coefficient C_f distribution over the airfoil suction and pressure surfaces at AoA = 5°. The separation and reattachment points can be identified at locations where C_f crosses zero. The boundary layer separation on the suction surface occurs at $x \sim 0.180$ and reattaches at $x \sim 0.585$, which shows strong agreement with the works of Jones *et al.*[39] A laminar separation bubble of a length 0.4 is observed at the selected flow condition whereas no boundary layer separation on the pressure surface is observed. A wavy pattern is observed downstream of the

TABLE I. Mesh parameters for the complete domain (min mesh size/max mesh size).

Physical domain					Buffer
$x < -1$	$-1 \leq x \leq 2$	$x > 2$	$\lvert y \rvert > 0.3$	$-0.3 \leq y \leq 0.3$	For all x, y
0.01/0.02	0.001/0.008	0.008/0.01	0.005/0.02	0.0007/0.008	0.02/0.1

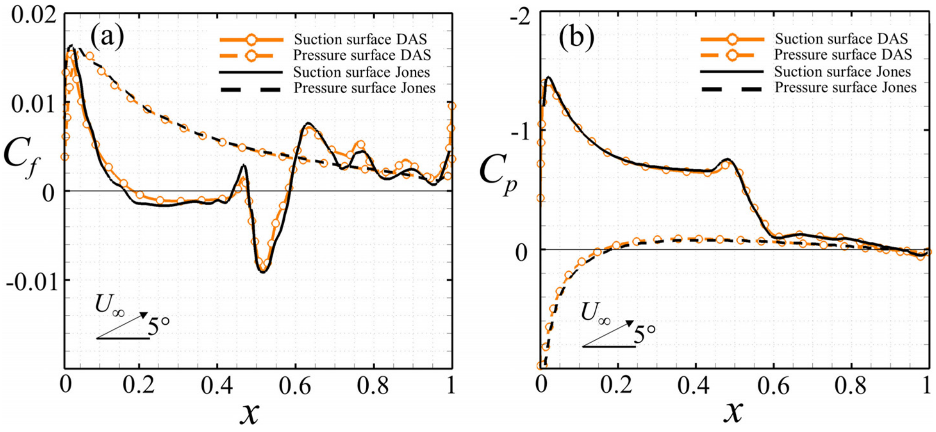

FIG. 2. Comparison of (a) time-averaged C_f distribution and (b) time-averaged C_p distribution over the airfoil at AoA = 5° with Jones *et al.*[39]

reattachment point, which exhibits periodic vortex shedding over the airfoil surface and is also reported in literature.[3,39,53]

Figure 2(b) shows the time-averaged pressure coefficient C_p over the suction and pressure surfaces of airfoil at AoA = 5°. On the suction surface, a sudden increase in C_p near the leading edge $0.04 < x < 0.2$ due to strong adverse pressure gradient can be observed. This is followed by a pressure plateau from $0.2 < x < 0.45$ and a rapid transition from $0.45 < x < 0.6$. From $0.6 < x < 0.79$, another pressure plateau is observed, which is followed by an increase in C_p up till trailing edge. C_p on the pressure surface decreases smoothly from the airfoil leading edge up to $x \sim 0.3$ and increases slowly up till the airfoil trailing edge. An excellent agreement with the works of Jones *et al.*[39] is observed with a maximum deviation of less than 2% in the airfoil C_p distribution.

F. Design and analysis methodology

The present study focuses on the reduction of tonal component of airfoil self-noise associated with the operations of low *Re* aerodynamic devices and is much higher than broadband noise in terms of magnitude. The airfoil is subjected to various loading conditions by means of varying the flow AoA and its effectiveness in tonal noise reduction is evaluated. A range of AoA is initially chosen over which the airfoil tonal noise is observed for a commonly used low *Re* airfoil such as NACA 0012.[4,40] According to McAlpine *et al.*,[9] the airfoil tonal noise would not be observed if the transition to turbulence occurred sufficiently far from the airfoil trailing edge. For the present study, the maximum limit of AoA is set to 7° as the boundary layer tends to be turbulent in its characteristics above this AoA for NACA 0012 airfoil,[38–40] and the generated airfoil noise tends to be broadband in nature. On the other hand, the minimum AoA is set to 3° below, in which the boundary layer separation occurs near the trailing edge of the airfoil and fails to reattach with the airfoil surface on both the pressure and suction surfaces.[4,39] It is not practically feasible to evaluate the effectiveness of an airfoil configuration with such a vast design space (based on multiple compliant panels) in noise reduction at each AoA. Therefore, an interval of 2° is maintained for the analysis within a range of AoA between 3° and 7°.

The adopted methodology for the design of DSC airfoil is divided into three major stages. Initially, the flow characteristics of the RS airfoil at selected AoAs are analyzed individually by DAS. The results of DAS analyses also serve as the base flow for subsequent PEM analyses. In the next stage, airfoil configuration mounted with single elastic panel (SEP) is designed for each AoA. The structural properties and suitable location of the panel on the airfoil surface are determined based on the RS airfoil characteristics. Subsequently, the effectiveness of the SEP configurations in tonal noise reduction is determined by PEM at their respective AoAs. Finally, a conceptual design of an airfoil mounted with three unique elastic panels is presented, which is aimed to provide tonal noise reduction over entire range of AoA. A comprehensive aeroacoustic DAS analysis is carried out for the DSC airfoil to evaluate its effectiveness in airfoil noise reduction and understand the underlying physical mechanisms.

III. RIGID SURFACE AIRFOIL ANALYSIS

The time-averaged C_f distributions over the airfoil suction and pressure surfaces at different AoAs are shown in Figs. 3(a) and 3(b), respectively. On the airfoil suction surface, the boundary layer separation occurs at $x \sim 0.34$ and reattaches at $x \sim 0.85$ at AoA = 3°; whereas, at AoA = 5°, the flow separation and reattachment shift upstream to $x \sim 0.18$ and $x \sim 0.58$, respectively. At higher AoA of 7°, the flow separation and reattachment points further shift toward airfoil leading edge at $x \sim 0.05$ and $x \sim 0.38$, respectively.[40] No boundary layer separation on the pressure surface is observed at any flow condition considered in this study. Figures 3(c) and 3(d) show the time-averaged C_p distribution over the suction and pressure surfaces of airfoil. For AoA = 3°, a sudden increase in C_p near the leading edge due to strong adverse pressure gradient can be observed on the airfoil suction surface. This is followed by a pressure plateau from $0.2 < x < 0.7$, and a rapid transition from $0.7 < x < 0.8$. From $0.8 < x < 0.9$, another pressure plateau is observed, which is followed by an increase in C_p up till airfoil trailing edge. The C_p on the pressure surface decreases smoothly from the airfoil leading edge up to $x \sim 0.25$ and remains constant up till $x \sim 0.6$ and then increases slowly up till airfoil trailing edge. Similar patterns of C_p variation are observed for AoA = 5° and 7° with much higher magnitudes and shorter lengths of pressure plateau, respectively, which indicate a reduction in the length of LSB at higher flow incidence. At the airfoil pressure surface, a similar trend of C_p distribution is observed for all AoAs.

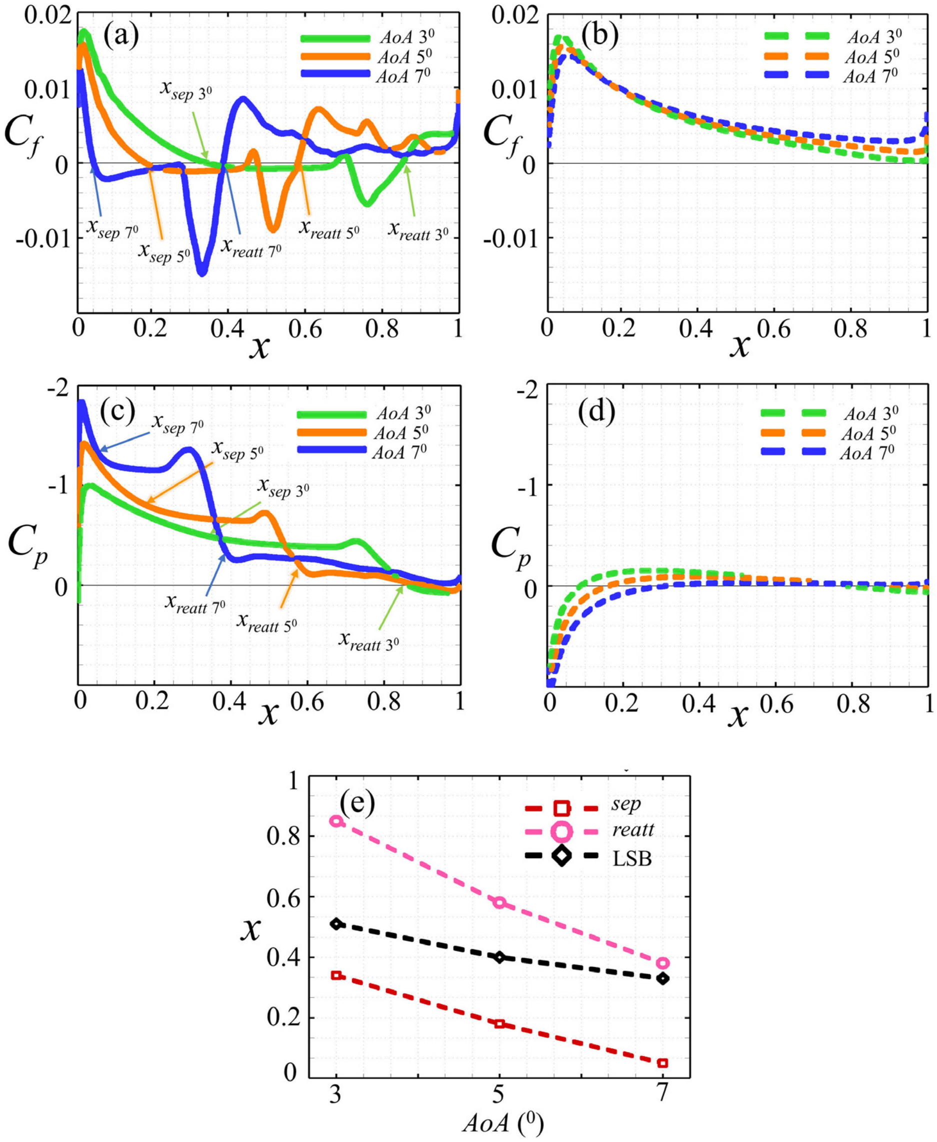

FIG. 3. Time-averaged C_f distribution over the airfoil (a) suction surface; (b) pressure surface. Time-averaged C_p distribution over the airfoil (c) suction surface; (d) pressure surface; and (e) variation of boundary layer separation and reattachment locations with AoA.

TABLE II. Comparison of time-averaged aerodynamic parameters. The term in brackets indicate the percentage deviation of the present DAS results from Jones *et al.*[39]

	From present DAS/From Jones *et al.*[39]		
Parameters	AoA = 3°	AoA = 5°	AoA = 7°
$C_{L,mean}$	0.430/0.425 (+1.17%)	0.485/0.490 (−1.02%)	0.650/0.640 (+1.56%)
$C_{D,mean}$	0.017/0.018 (−5.55%)	0.0185/ 0.0201 (−7.96%)	0.040/0.041 (−2.43%)
x_{sep}	0.34/0.33 (+3.03%)	0.18/0.16 (+11.1%)	0.05/0.05 (−)
x_{reatt}	0.85/0.85 (−)	0.58/0.58 (−)	0.38/0.39 (−2.56%)
LSB	0.51/0.52 (−1.92%)	0.40/0.43 (−6.97%)	0.33/0.34 (−2.94%)
$f_{dominant}$	2.67/2.42 (+10.33%)	3.37/3.37 (−)	2.40/2.40 (−)

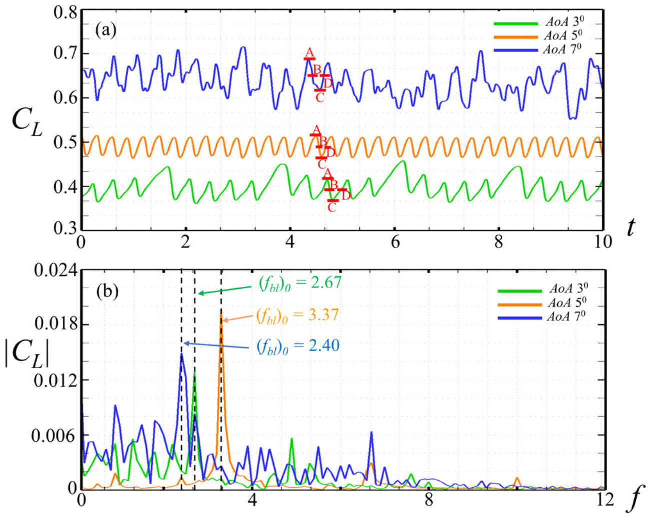

FIG. 4. (a) C_L variation with time; and (b) FFT spectra of C_L.

The variations in the separation/reattachment points and length of LSB with increasing AoA are shown in Fig. 3(e). The figure clearly indicates an upstream shift of the LSB and its shrinkage from $\Delta x = 0.51$ to 0.33 with an increase in AoA from 3° to 7°. Table II presents a summary of the calculated time-averaged aerodynamic parameters for all AoAs alongside with their comparison with available literature. A good agreement is observed in the calculated parameters at all conditions with literature,[39] which further validates the numerical methodology adopted for the study.

The variations of the coefficient of lift C_L with time ($t = \hat{t}\hat{U}_\infty/\hat{c}$) for all AoAs are shown in Fig. 4(a). The C_L fluctuates essentially in a periodic manner for lower AoAs (i.e., $\leq 5°$), whereas its variation becomes irregular at higher *AoA* indicating the presence of complex unsteady flow behavior.[38] Figure 4(b) shows the results of Fast Fourier Transform (FFT) of C_L for all *AoAs*. A time episode of $t = 10$ with a non-dimensional sampling frequency ($f = \hat{f}\hat{c}/\hat{U}_\infty$) of 1×10^5 for fine resolution is utilized with a Hamming window with 50% data overlap for the transform. The FFT spectrum for AoA $= 3°$ indicates a clear dominant peak frequency of 2.67 with several low amplitude peaks associated with higher-harmonics. At AoA $= 5°$, the spectrum reveals a dominant peak frequency of 3.37 along with higher harmonics at 6.6 and 10.0. However, at AoA $= 7°$, the spectrum exhibits a scattered spectrum with different low amplitude peaks at irregular intervals. The highest magnitude peak is observed at the frequency of 2.40.

According to Lighthill's acoustic analogy,[54] the unsteady motions of vortices convecting over the airfoil generate noise, which is similar to the scattering of an incident wave at a sharp edge. The passage of vortical structures over the airfoil trailing edge into the wake generally creates discrete tones.[55,56] Hence, it is informative to visualize the flow field sequence of vortex shedding over the airfoil to investigate the noise generation mechanism. Figure 5 illustrates the evolution of vorticity distribution within a single lift cycle for every AoA. The time instances chosen correspond to A, B, C, and D shown in Fig. 4(a). The point A represents the instance of maximum lift for each AoA, whereas the time instance of C indicates the point of minimum lift. On the other hand, points B and D indicate the locations of the lift cycle where it crosses the neutral axis locally. The black dashed line indicates the convection of a single vortex over the complete lift cycle for each AoA. For AoA $= 3°$, the flow unsteadiness over the airfoil suction surface results in the vortex generation from the separated shear layer on airfoil suction surface and its passage over the airfoil trailing edge into the wake. The vortex shedding appears to be periodic with strong coherent structures convecting toward the airfoil trailing

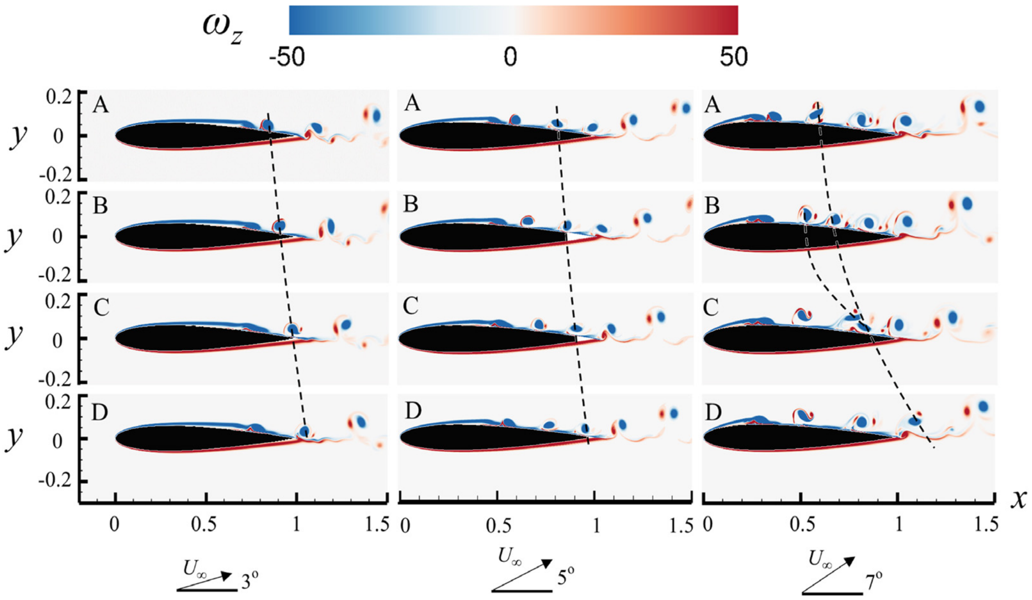

FIG. 5. Temporal evolution of vorticity distribution at different AoAs. Time instances A–D are referred to Fig. 4(a).

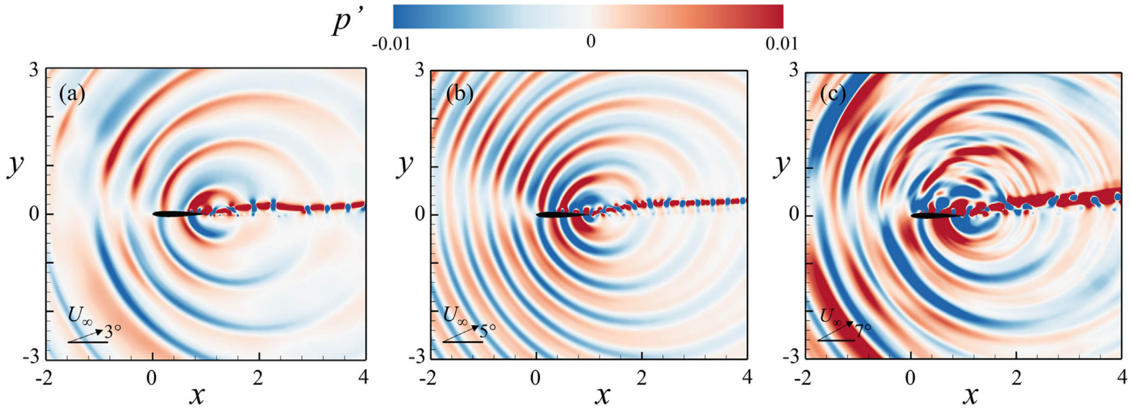

FIG. 6. Instantaneous acoustic pressure fluctuations p' at the time instances of maximum lift at each AoA. (a) AoA = 3°; (b) AoA = 5°; and (c) AoA = 7°.

edge as indicated by the dashed black line. For AoA = 5°, the emergence of the vortices shift upstream with an increase in AoA due to the variation in the locations of separation and reattachment points as observed in Fig. 3(a). Again, the vortex shedding appears to be periodic with strong coherent structures shedding into the airfoil wake. On the other hand, for AoA = 7°, the vortex shedding appears to be non-periodic, and vortex merging is observed at time instance C where two vortices coalesce and promote high levels of flow instabilities over the later half of airfoil. This non-coherent vortex shedding at AoA = 7° is found to be responsible for the presence of multiple peaks in the FFT spectra as observed in Fig. 4(b).[57,58]

Figure 6 shows the instantaneous fluctuating pressure p', defined by $p'(x,t) = p(x,t) - p_{mean}(x)$, at the time instance of maximum lift for each AoA. Regions of prominent instabilities on the suction surface of the airfoil can be observed for all cases. For each loading condition, acoustic waves originate from the trailing edge and propagate upstream with a much higher magnitude than those in the downstream direction. The strength of acoustic radiation appears to be higher at AoA = 7° as compared with lower AoAs (i.e., ≤ 5°). The radiation patterns for lower AoAs are observed to be similar where the acoustic waves appear to radiate in a uniform pattern with a phase difference of 180° between the suction and pressure surfaces over the

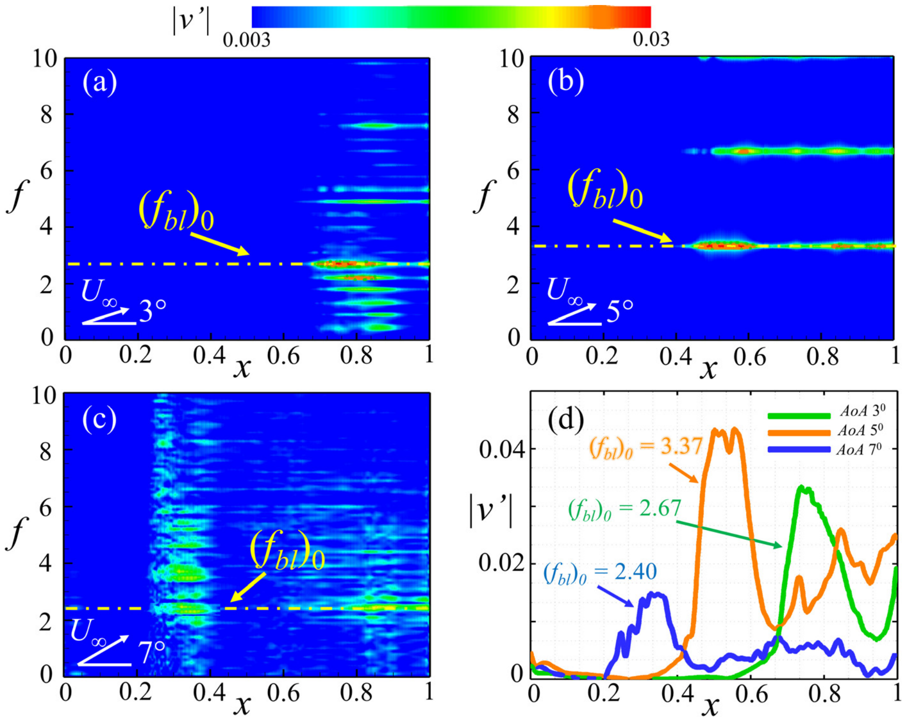

FIG. 7. Distribution of spectra of transverse velocity fluctuations along the airfoil. (a) AoA = 3°; (b) AoA = 5°; and (c) AoA = 7°. (d) Spatial growth of flow instability over the airfoil suction surface at $(f_{bl})_0$.

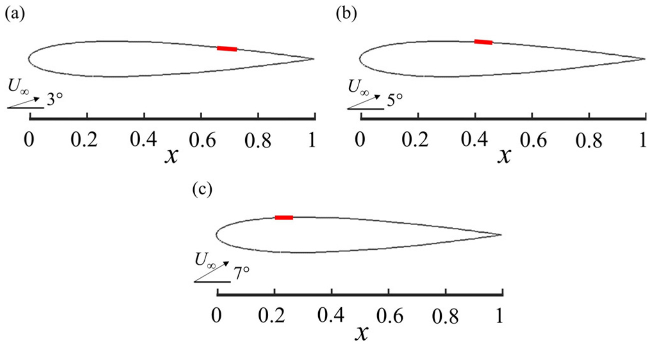

FIG. 8. Schematics of designed SEP configurations. (a) SEP3; (b) SEP5; and (c) SEP7.

airfoil [Figs. 6(a) and 6(b)]. However, at higher AoA [Fig. 6(c)], the acoustic radiation appears to be non-uniform due to non-uniform vortex shedding occurring over the airfoil suction surface as observed in Fig. 5.

IV. DESIGN OF ELASTIC PANELS

A. Design of single elastic panel configurations

The airfoil configurations with single elastic panel (SEP) are designed for different AoAs by utilizing the corresponding RS airfoil analysis, and the effectiveness of these configurations in tonal noise reduction is determined by PEM. The design of elastic panel is essentially based on three major parameters, namely panel length, structural properties, and its location. The length of panel is set as $L_{\mathrm{EP}} = 0.05$ for all the cases as such short length does not affect the radius of curvature over the airfoil suction surface.[47] In fact, a longer panel with much longer structural wavelength than the acoustic wavelength may become a noise source itself and radiate energy into the fluid and far-field.[59] To determine the suitable locations of panel for the AoAs, the frequency spectra of transverse velocity fluctuations v' over the airfoil suction surface within the boundary layer are analyzed and shown in Figs. 7(a)–7(c). In these figures, a longer time history of $t = 20$ and a higher sampling frequency of 2×10^5 are selected for fine spectral resolution. The horizontal dot-dashed lines indicate the dominant frequencies of the boundary layer instabilities. For AoA = 3° [Fig. 7(a)], its spectrum reveals that the natural airfoil boundary layer growth is dominated by the fundamental frequency $(f_{bl})_0 = 2.67$ along with its harmonics at the $(f_{bl})_1 = 5.20$. The magnitude of v' becomes observable within $0.65 \le x \le 0.85$, which indicates the presence of significant boundary layer instabilities within the separation bubble. The magnitude of v' observed at the fundamental frequency $(f_{bl})_0 = 2.67$ is much higher than its first harmonics at $(f_{bl})_1 = 5.20$. Some moderate amplitude flow fluctuations are also observed at $f = 2.20$ and 1.70, which possibly indicate the presence of secondary tones.[4,57] For AoA = 5° [Fig. 7(b)], the spectrum reveals that the natural airfoil boundary layer growth is dominated by the fundamental frequency $(f_{bl})_0 = 3.37$ along with its higher harmonics. The magnitude of v' becomes observable from $x \sim 0.4$ up to the airfoil trailing edge, which indicates the presence of significant boundary layer instabilities; whereas, for AoA = 7° [Fig. 7(c)], the spectrum shows scattered frequency content as also observed in Fig. 4(b). However, a high magnitude of v' is observed at $(f_{bl})_0 = 2.40$. The magnitude becomes observable within $0.2 \le x \le 0.38$ within the separation bubble and reduces significantly at the reattachment point. The magnitude slightly increases again at a downstream location near the airfoil trailing edge. Some moderate amplitude flow fluctuations are also observed at $f = 2.0$ and 3.60 at this AoA.

To investigate the unsteady flow behavior within the boundary layer over the suction surface, the natural boundary layer stability characteristics are analyzed at the dominant frequencies for AoA = 3° ($(f_{bl})_0 = 2.67$), AoA = 5° ($(f_{bl})_0 = 3.37$), and AoA = 7° ($(f_{bl})_0 = 2.40$) as shown in Fig. 7(d). For AoA = 3°, the amplitude of v' starts to increase at $x \ge 0.55$ and grow within $0.65 \le x \le 0.7$ whereas the amplitude of v' for AoA = 5° starts to increase at $x \ge 0.27$ and grow within $0.4 \le x \le 0.45$. For AoA = 7°, the growth of v' moves further upstream where it starts to increase at $x \ge 0.18$ and grow within $0.2 \le x \le 0.32$. It is well established that a resonant elastic panel is able to effectively weaken the boundary layer instabilities when it is located corresponding to the onset of rapid growth of flow instabilities.[47] Based on the flow instability characteristics over the suction surface of airfoil observed in Fig. 7(d), the panel for the case of AoA = 3° is located with its leading edge at $x_{le} = 0.65$ on the airfoil suction surface (designated as SEP3). The location of the panel for the case of AoA = 5° is set with its leading edge at $x_{le} = 0.40$ on the airfoil suction surface (SEP5); and for the case of AoA = 7°, the panel is located with its leading edge at $x_{le} = 0.20$ on the airfoil suction surface (SEP7). The schematics of the airfoil with single elastic panel for all AoAs are shown in Figs. 8(a)–8(c).

For each case, the properties of the panel are selected in a way that its natural frequency coincides with the dominant frequency of the flow instabilities within the boundary layer to achieve structural resonance condition in its third natural mode under the fluid loading. The normalized frequency of the nth panel vibration mode can be estimated as[60]

$$(f_{\mathrm{EP}})_n = \frac{n}{2L_{\mathrm{EP}}}\sqrt{\frac{T_{\mathrm{EP}}}{\rho_{\mathrm{EP}} h_{\mathrm{EP}}}} \bigg/ \sqrt{1 + \frac{L_{\mathrm{EP}}}{\pi n \rho_{\mathrm{EP}} h_{\mathrm{EP}}}}. \qquad (6)$$

The selected parameters for the designed panel in non-dimensional form are tabulated in Table III.

TABLE III. Normalized elastic panel parameters.

Case	x_{le}	L_{EP}	h_{EP}	T_{EP}	ρ_{EP}	$(f_{\mathrm{EP}})_1$	$(f_{\mathrm{EP}})_2$	$(f_{\mathrm{EP}})_3$	$(f_{\mathrm{EP}})_4$	$(f_{\mathrm{EP}})_5$
SEP3	0.65	0.05	0.014	0.725	6367.34	0.89	1.78	2.67	3.56	4.45
SEP5	0.40	0.05	0.009	0.725	6367.34	1.12	2.24	3.37	4.49	5.62
SEP7	0.20	0.05	0.009	0.366	6367.34	0.81	1.61	2.40	3.20	4.01

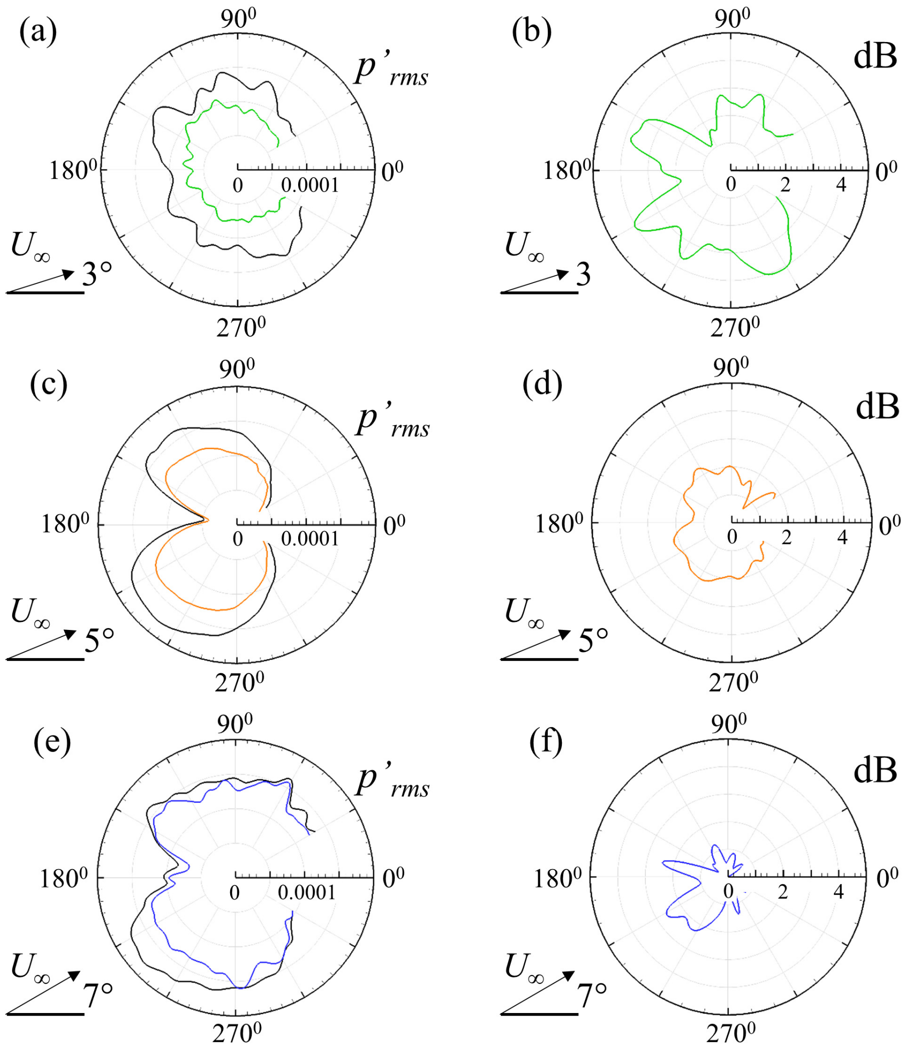

FIG. 9. Azimuth distribution of p'_{rms} at $r = 3$. (a) AoA = 3°; (c) AoA = 5°; and (e) AoA = 7°. Azimuth distribution of ΔSPL at $r = 3$. (b) AoA = 3°; (d) AoA = 5°; and (f) AoA = 7°. Green solid line, SEP3; orange solid line, SEP5; blue solid line, SEP7; black solid line, RS airfoil at the corresponding AoA.

B. Assessment of noise reduction through reduced order modeling

A quick assessment of noise reduction potential of the SEP configurations at AoA = 3° and 5° and 7° is carried out by reduced order modeling. The azimuth plots of p'_{rms} at $r = 3$ for all AoAs are shown in Figs. 9(a), 9(c), and 9(e). The acoustic solution within the sector $|\theta| \leq 30°$ is ignored due to strong contamination of aerodynamic pressure fluctuations downstream of the airfoil trailing edge, which makes the determination of acoustics inaccurate at these locations. For each AoA, the noise directivity resembles its corresponding RS airfoil, which confirms that the panel vibration does not affect the mean flow dynamics. For SEP3, the strongest radiation goes along $\theta \sim 140°$ and $\sim 300°$, respectively; whereas, for SEP5, the strongest radiation goes along $\theta \sim 150°$ and $\sim 240°$, respectively. A significant reduction in p'_{rms} is observed at all azimuth locations for SEP3 and SEP5 as compared

TABLE IV. Noise-reduction effectiveness of SEP configurations at different flow conditions.

	AoA = 3°		AoA = 5°		AoA = 7°	
Case	Avg ΔSPL (dB)	Max ΔSPL (dB)	Avg ΔSPL (dB)	Max ΔSPL (dB)	Avg ΔSPL (dB)	Max ΔSPL (dB)
SEP3	3.50	5.60	0.60	0.81	0.20	0.32
SEP5	0.57	0.73	2.10	2.40	0.66	0.81
SEP7	0.04	0.06	0.09	0.10	1.10	2.70

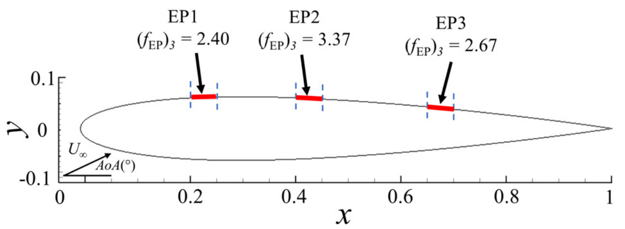

FIG. 10. Schematic sketch of the DSC airfoil design concept.

TABLE V. Comparison of lift to drag ratio for RS and DSC airfoils.

Case	AoA = 3°	AoA = 5°	AoA = 7°
RS	26.47	26.24	15.99
DSC	26.18	26.03	15.68
Percentage deviation from RS	−1.09%	−0.80%	−1.93%

with the RS airfoil at the corresponding AoAs. For SEP7, the strongest radiation goes along $\theta \sim 140^\circ$ and $\sim 220^\circ$, respectively. The reduction in p'_{rms} for SEP7 appears to be much lower than other configurations.

The extent of noise reduction by each SEP configuration is illustrated by evaluating the reduction in overall sound pressure level, defined by $\Delta SPL = -20 \times \log_{10}(p'_{rms,\mathrm{SEP}}/p'_{rms,\mathrm{RS}})$, as shown in Figs. 9(b), 9(d), and 9(f). Different extent of noise reduction is observed for each configuration around all azimuth locations. Table IV shows the comparative analysis of noise reduction for all configurations at all AoAs. The shaded cells in Table IV indicate the noise reduction effectiveness of the SEP configurations at their designed AoAs. The noise reduction potential of each SEP configuration at their off-design AoAs is also shown in Table IV to analyze their effectiveness at different loading conditions. An average ΔSPL reduction of 3.5 dB is observed for SEP3 at AoA = 3° with a maximum reduction of ∼5.6 dB. Such significant noise reduction performance of SEP3 at AoA = 3° can be attributed to the presence of longer separation bubble ($x \sim 0.51$) as compared with the separation bubbles observed at AoA = 5° and 7°, respectively, which allows the panel to transfer higher energy from the flow insatiabilities within the separated region to sustain its vibration. However, as envisaged, the noise reduction potential of SEP3 at other AoAs is considerably affected where the

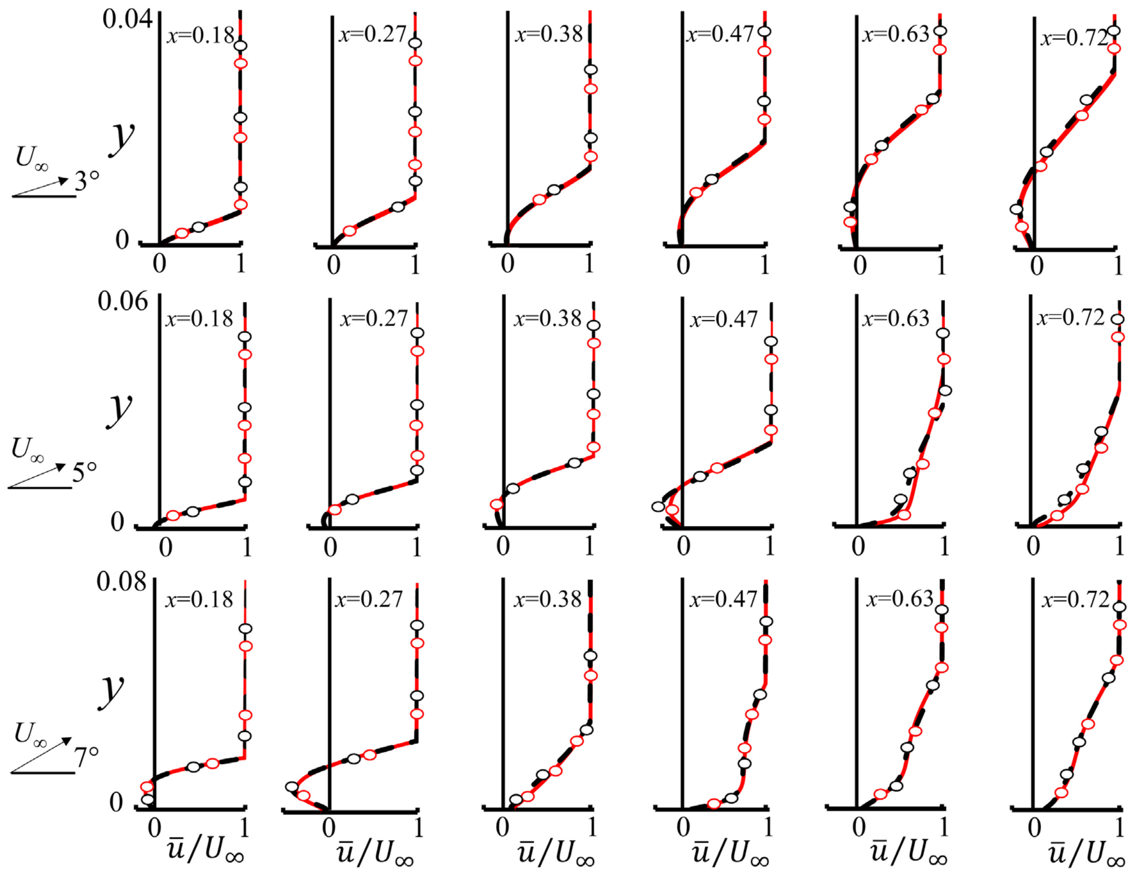

FIG. 11. Time-averaged streamwise velocity profiles for RS and DSC airfoils over the suction surface at different chord locations. Dotted line, RS airfoil; red solid line, DSC airfoil.

average and maximum Δ*SPL* reduction at AoA = 5° drops to 0.6 and 0.8 dB, respectively. Whereas, the average and maximum Δ*SPL* reduction for SEP3 at AoA = 7° further drops to 0.2 and 0.3 dB, respectively. For SEP5 configuration at AoA = 5°, an average noise reduction of 2.1 dB is observed with a maximum reduction of 2.4 dB. Similar to SEP3, the noise reduction potential of SEP5 is also degraded at AoA = 3° and AoA = 7° as shown in Table IV. The extent of noise reduction for SEP7 configuration at AoA = 7° is much lower than other configurations where an average noise reduction of only 1.1 dB is observed. Furthermore, the SEP7 configuration provides almost no noise reduction at AoA = 3° and AoA = 5°, respectively. It is important to note that although the noise reduction effectiveness of SEP configurations is reduced at their off-design AoAs, no noise amplification is observed for any case.

PEM analyses of all SEP configurations evidently illustrate a significant tonal noise reduction for their designed AoAs as shaded in Table IV. However, the noise reduction potential of each configuration is severely affected at other AoAs, which would limit their feasibility and usability in different loading conditions. To overcome this limitation, a distributed surface compliance (DSC) airfoil is proposed, which could provide considerable tonal noise reduction at various loading conditions.

V. DISTRIBUTED SURFACE COMPLIANCE AIRFOIL

A. Design concept

In the present study, a design concept for DSC airfoil is proposed by mounting three unique elastic panels, with structural properties devised in respective SEP configurations, on its suction surface (Fig. 10). The proposed design scheme of DSC airfoil is intended to cater for variation in flow AoA by employing the elastic panels at critical locations that can help in the suppression of flow insatiabilities at each AoA. The first elastic panel (designated as "EP1") is located with its leading edge at $x_{le} = 0.2$ based on the favorable noise reduction characteristics of SEP7 observed at AoA = 7°; the second elastic panel (designated as "EP2") is located with its leading edge at $x_{le} = 0.4$ based on the favorable noise reduction characteristics of SEP5 at AoA = 5°; and the third elastic panel (designated as "EP3") is located with its leading edge at $x_{le} = 0.65$ due to its high noise reduction potential of SEP3 at

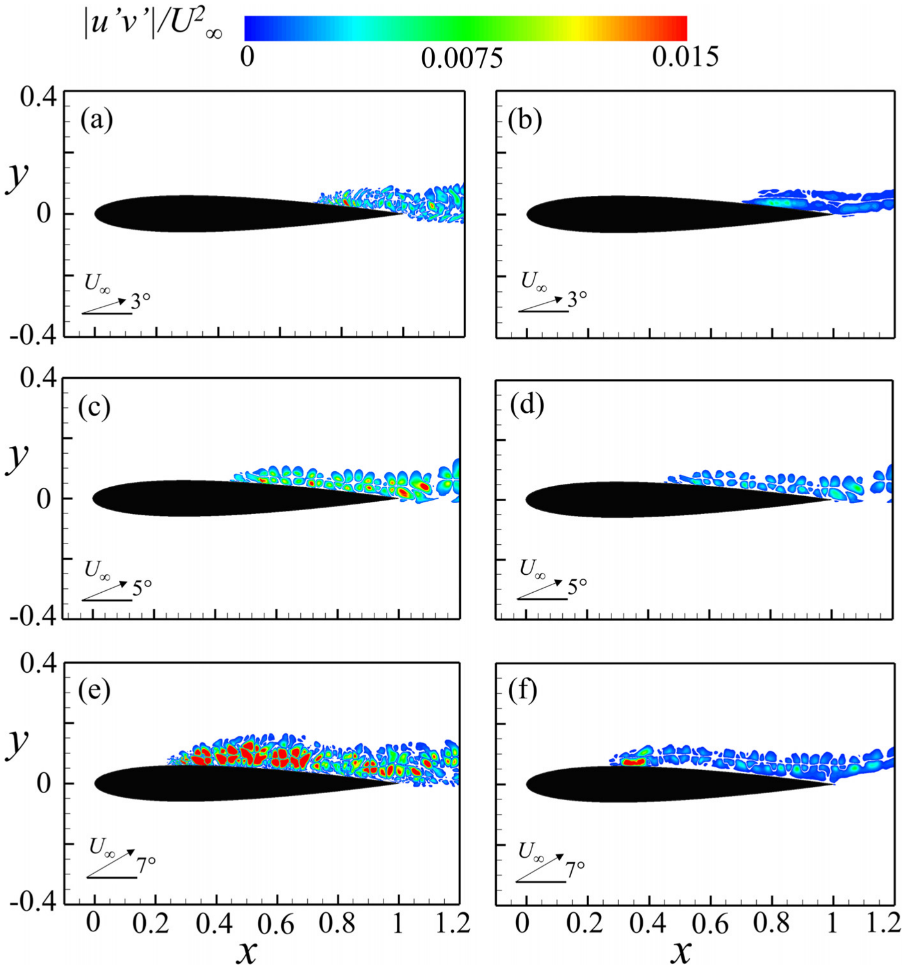

FIG. 12. Distribution of Reynolds stress over RS airfoil (left column) and DSC airfoil (right column). (a) and (b), AoA = 3°; (c) and (d), AoA = 5°; and (e) and (f), AoA = 7°.

AoA = 3° as presented in Table IV. The structural properties and the natural frequencies of each elastic panel are different where the properties of EP1 corresponds to the elastic panel utilized for SEP7, EP2 corresponds to the panel properties of SEP5, and EP3 corresponds to the panel properties of SEP3 as shown in Table III.

B. DAS analysis of DSC airfoil

The capability of DSC airfoil in tonal noise reduction at various loading conditions is evaluated by high-fidelity DAS analysis. The complex interdynamical structural interaction among the panels and their effects on airfoil aerodynamics and acoustics are also explored in detail to uncover the mechanisms responsible for noise reduction. A comparative analysis of DSC airfoil with RS airfoil is also carried out to ascertain the modification in aeroacoustics characteristics of the airfoil due to the presence of elastic panels.

1. Airfoil flow field analysis

To analyze the effect of panels dynamics on the airfoil hydrodynamics, the time-averaged streamwise boundary layer profiles for both RS and DSC airfoils are analyzed over the suction surface at different airfoil chord locations. The chord locations are carefully selected to ascertain the impact of panel vibrations on the boundary layer

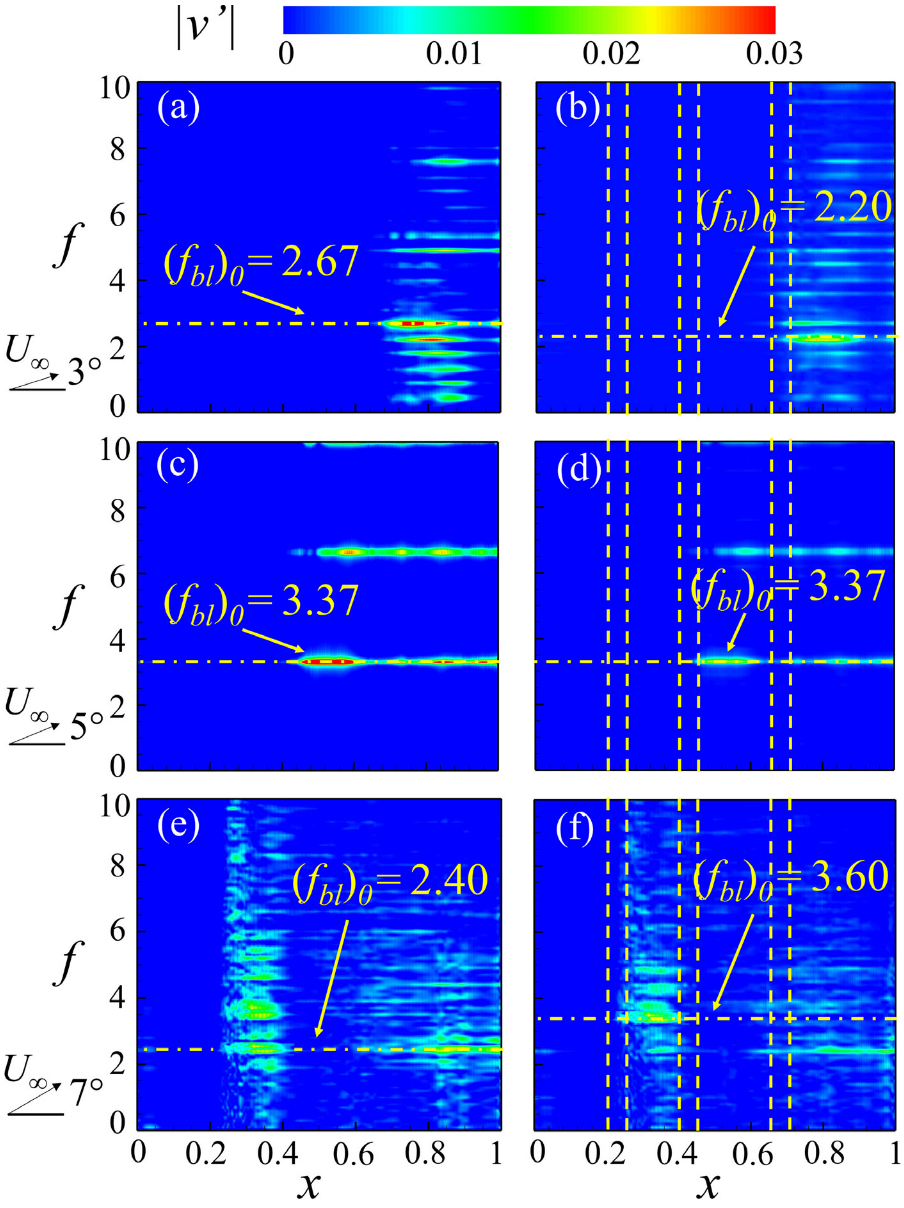

FIG. 13. Distribution of spectra of transverse velocity fluctuations over RS airfoil (left column) and DSC airfoil (right column). (a) and (b), AoA = 3°; (c) and (d), AoA = 5°; and (e) and (f), AoA = 7°. The vertical dashed lines indicate the coverage of panels for DSC airfoil.

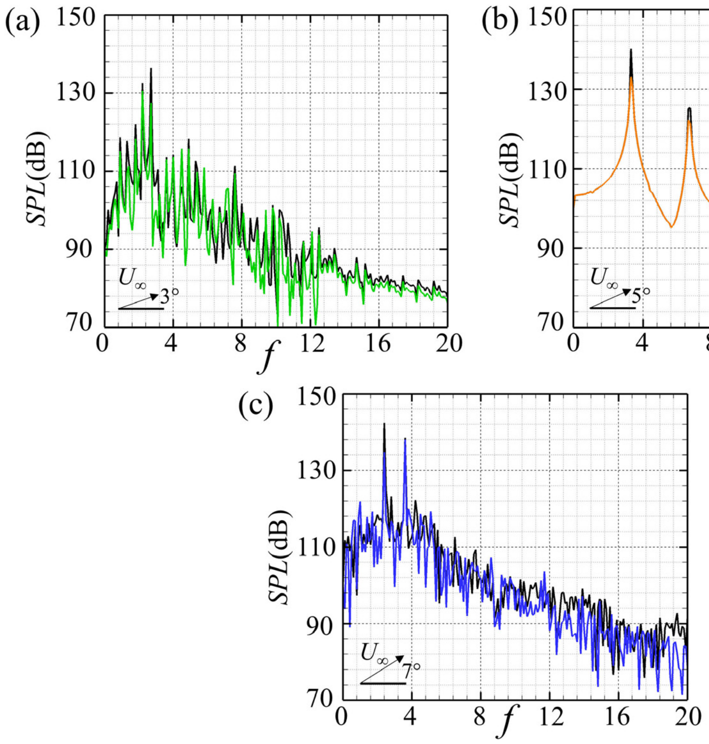

FIG. 14. Comparison of SPL spectra between RS and DSC airfoils at $(x, y) = (1, 2)$. (a) AoA $= 3°$; (b) AoA $= 5°$; and (c) AoA $= 7°$. Green solid line/orange solid line/blue solid line, DSC airfoil; black solid line, RS airfoil at the corresponding AoA. The reference acoustic pressure for SPL is taken as 2×10^{-5} Pa.

characteristics in its near vicinity with an offset of $\Delta x = 0.02$ before and after the panel edges; i.e., $x = 0.18$, 0.27, 0.38, 0.47, 0.63, and 0.72. From Fig. 11, it is evident that the boundary layer thickness grows significantly with an increase in AoA. Furthermore, a prominent effect of flow separation and adverse pressure gradient can be observed due to the formation of separation bubble, i.e., $0.34 < x < 0.85$ for AoA $= 3°$, $0.18 < x < 0.58$ for AoA $= 5°$, and $0.05 < x < 0.38$ for AoA $= 7°$. The profiles for both RS and DSC airfoils are almost identical prior to the formation of separation bubble at all AoAs. However, a slight difference is observed in the lower half of boundary layer within the separation bubble where the thickness of boundary layer is slightly reduced and an increase in the near-wall velocity is observed for DSC airfoil with less intensive reverse flow for all AoAs. This implies that the boundary layer is reattached to the suction surface at an upstream location for DSC airfoil as compared to RS airfoil. Also, the reduction in the thickness of boundary layer for DSC airfoil would ultimately result in a narrower wake as compared with RS airfoil.[4,61,62]

The aerodynamic efficiency of the RS airfoil and DSC airfoil is compared by evaluating the time-averaged lift to drag $C_{L,mean}/C_{D,mean}$ at each AoA (Table V). The analysis reveals that the DSC airfoil can operate over a wide range of AoA with negligible sacrifice in the airfoil performance. Compared with the RS airfoil, the aerodynamic efficiency of DSC airfoil varies by only 1.09%, 0.80%, and 1.93% for AoA $= 3°$, $5°$, and $7°$, respectively, which is much lower than the loss of aerodynamic efficiency observed for membrane airfoils operating at similar flow conditions AoA (~21%).[63]

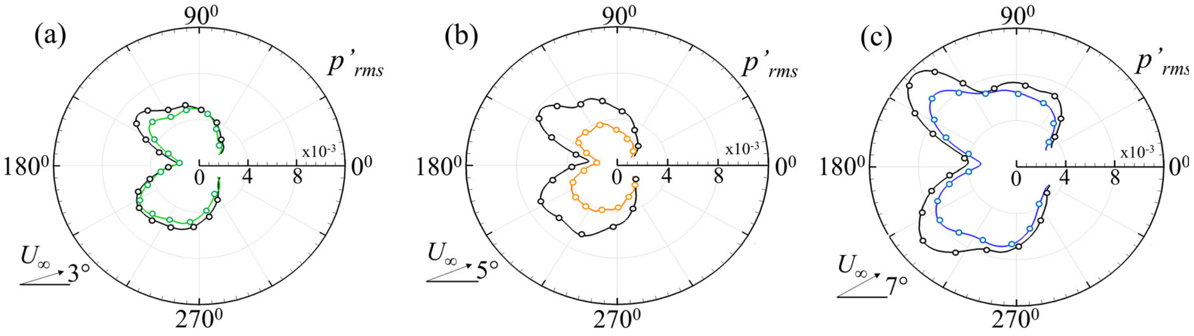

FIG. 15. Comparison of azimuth distributions of p'_{rms} at $r = 3$. (a) AoA $= 3°$; (b) AoA $= 5°$; and (c) AoA $= 7°$.Green solid line/orange solid line/blue solid line, DSC airfoil; black solid line, RS airfoil at the corresponding AoA.

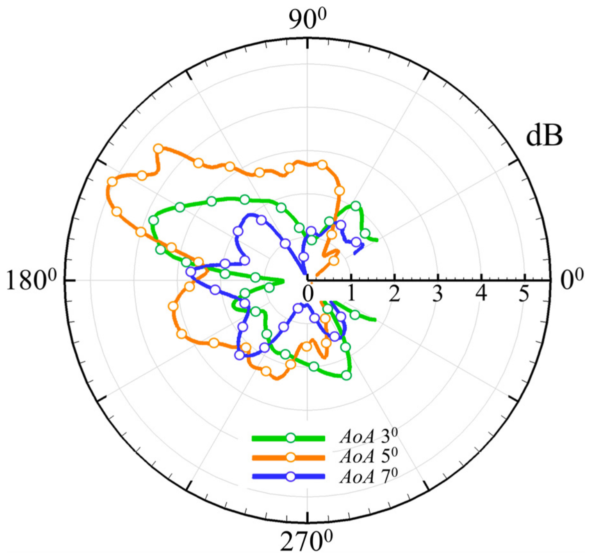

FIG. 16. Azimuth distribution of ΔSPL at $r = 3$ for DSC airfoil.

The contributions of flow fluctuations and their effect on additional momentum fluxes in the flow are investigated by evaluating the Reynolds stress magnitude $(|u'v'|/U_\infty^2)$ for RS and DSC airfoils at all AoAs and are shown in Fig. 12. For both the airfoils, the magnitude of fluctuations starts to grow near the boundary layer reattachment point and further increases toward the airfoil wake. This increase is attributed to the vortex shedding induced by the flow instabilities within the separation bubble.[4,5] However, a marked difference in the magnitudes of Reynolds stress can be observed for DSC airfoil [Figs. 12(b), 12(d) and 12(f)]. At AoA = 3° and 5°, the reduction in magnitude for DSC airfoil appears to be more pronounced than AoA = 7° as the flow tends to re-energize toward the trailing edge at higher AoAs.

The frequency spectra of transverse velocity fluctuations v' within the boundary layer for both RS and DSC airfoils are analyzed and shown in Fig. 13. The data sampling and frequency resolution are kept similar to Fig. 7 for comparative analysis. The horizontal dot-dashed lines indicate the dominant frequencies $(f_{bl})_0$ of the boundary layer instabilities; whereas the vertical dashed lines indicate the coverage of panels for DSC airfoil. For AoA = 3° [Figs. 13(a) and 13(b)], a significant reduction in the magnitude of v' is observed at $(f_{bl})_0 = 2.67$ for DSC airfoil, whereas the dominant frequency $(f_{bl})_0$ shifts to 2.20. Flow instabilities with moderate intensity were already observed at $f = 2.20$ for RS airfoil in Fig. 7(a), which indicate that the suppression of flow instabilities at $(f_{bl})_0 = 2.67$ by DSC airfoil results in the shift of dominant frequency to the next peak frequency. The peak magnitude of v' at $f = 2.20$ for DSC airfoil is observed to be much lower than that of $f = 2.67$ for RS airfoil and slightly lower than 2.20. Interestingly, no change in $(f_{bl})_0$ for DSC airfoil is observed at AoA = 5° [Figs. 13(c) and 13(d)] with a much pronounced reduction in the magnitude of v'. For AoA = 7°, a similar phenomenon to that of AoA = 3° is observed where a change in $(f_{bl})_0$ from 2.40 to 3.60 is observed for DSC airfoil. As observed in Fig. 7(c), flow insatiabilities of high strength are observed at both $f = 2.40$ and 3.60. Therefore, suppression of the flow insatiabilities at $f = 2.20$ results in a shift of dominant frequency to 3.60 for DSC airfoil. Only a slight reduction in the magnitudes of v' at $(f_{bl})_0 = 2.40$ for RS airfoil and $(f_{bl})_0 = 3.60$ for DSC airfoil is observed.

2. *Airfoil acoustics*

The acoustic characteristics of RS and DSC airfoils are evaluated and compared by analyzing their SPL spectra above the airfoil trailing edge at a location of $(x, y) = (1, 2)$ at each AoA and shown in Fig. 14. At AoA = 3°, a shift in the tonal noise frequency from $f = 2.67$ to

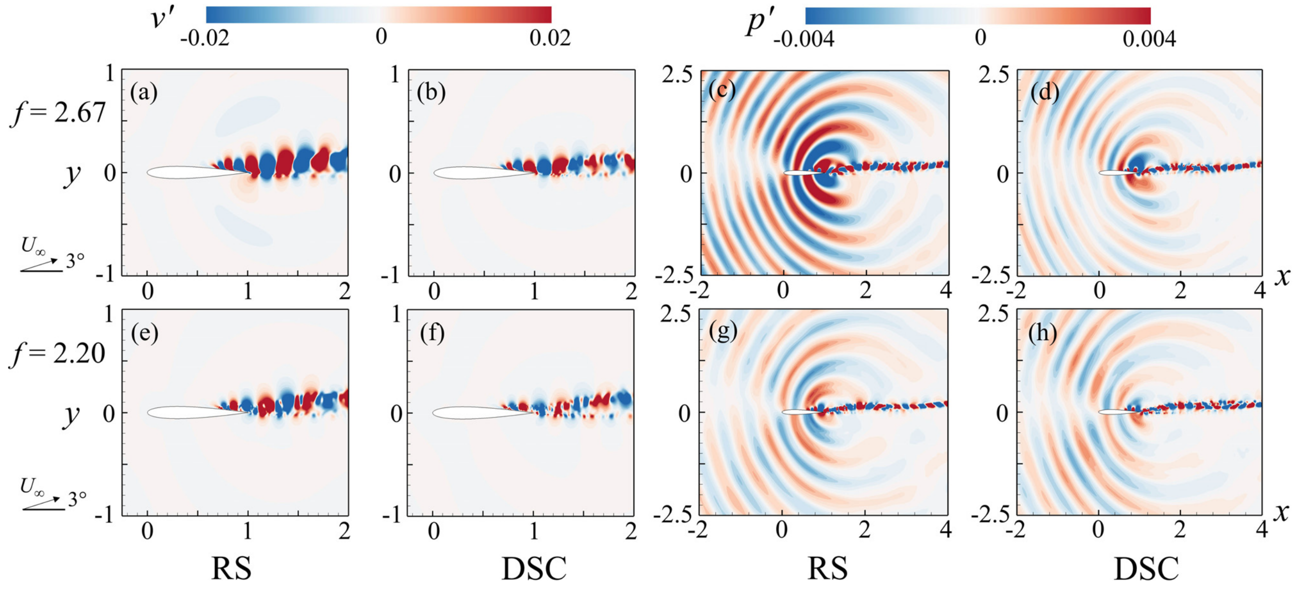

FIG. 17. Filtered FFT distribution of v' [i.e., (a), (b), (e), and (f)] and p' [i.e., (c), (d), (g), and (h)] at $f = 2.67$ (top row) and $f = 2.20$ (bottom row) for RS and DSC airfoils at $AoA = 3°$.

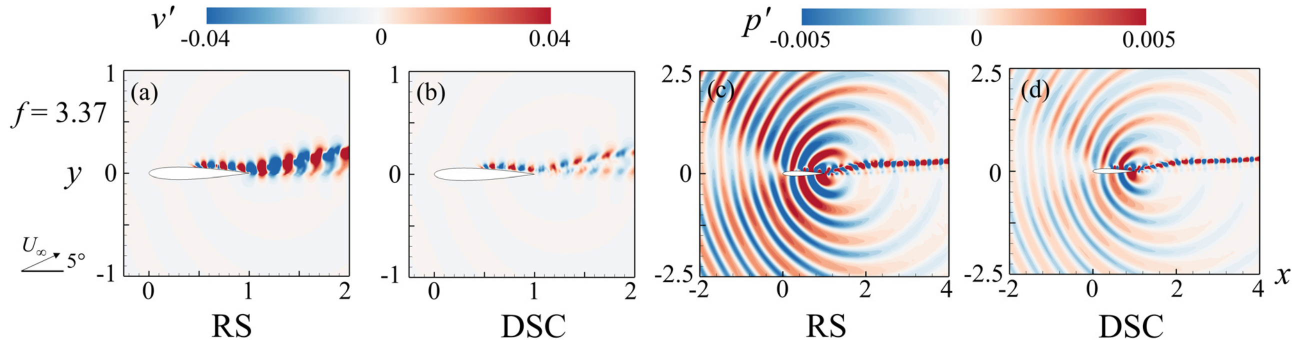

FIG. 18. Filtered FFT distribution of v' [i.e., (a) and (b)] and p' [i.e., (c) and (d)] at $f = 3.37$ for RS and DSC airfoils at AoA = 5°.

$f = 2.20$ is evident (cf. Fig. 13), and a maximum noise reduction of 5 dB is observed between peak-to-peak frequencies for the DSC airfoil. The spectra of both RS and DSC airfoils remain similar at AoA = 5° where a maximum noise reduction of 7 dB is observed for the DSC airfoil. At AoA = 7°, a shift in the peak frequency is observed again from $f = 2.40$ to $f = 3.60$ where a maximum noise reduction of 3 dB is observed between peak-to-peak frequencies for the DSC airfoil.

The effect of DSC airfoil on the acoustic radiation is analyzed by plotting the azimuth variations of p'_{rms} at $r = 3$ at each AoA (Fig. 15). At all AoAs, a reduction in the magnitude of p'_{rms} is observed for DSC airfoil, which affirms that the designed airfoil configuration can provide noise reduction at all loading conditions. At AoA = 3°, a significant reduction in p'_{rms} is observed in the second quadrant for DSC airfoil; whereas, a nominal reduction in p'_{rms} is observed in third and fourth quadrants. At AoA = 5°, the reduction in p'_{rms} is observed to be significant in all directions with much higher reduction toward the forward plane. However, at AoA = 7°, the reduction in magnitude is observed to be non-uniform.

Figure 16 shows the reduction in the overall sound pressure level ($\Delta \text{SPL} = -20 \times \log_{10}(p'_{rms,\text{DSC}}/p'_{rms,\text{RS}})$) for DSC airfoil evaluated at all AoAs. The overall noise reduction for DSC airfoil at AoA = 5° is observed to be much higher than other AoAs. At AoA = 5°, a maximum ΔSPL reduction of ∼5.04 dB is observed at $\theta = 154°$ whereas an average reduction of 2.21 dB is observed. At AoA = 3°, the maximum and average ΔSPL reduction of ∼3.83 dB (at $\theta = 158°$) and ∼1.81 dB is observed, respectively. The effectiveness of DSC airfoil in noise reduction slightly reduces at AoA = 7° where the maximum and average ΔSPL reduction of ∼2.69 dB (at $\theta = 175°$) and ∼1.34 dB is observed, respectively. The acoustic analysis clearly indicates that the DSC airfoil is highly effective in providing considerable airfoil tonal noise reduction at all AoAs as compared with single elastic panel configurations.

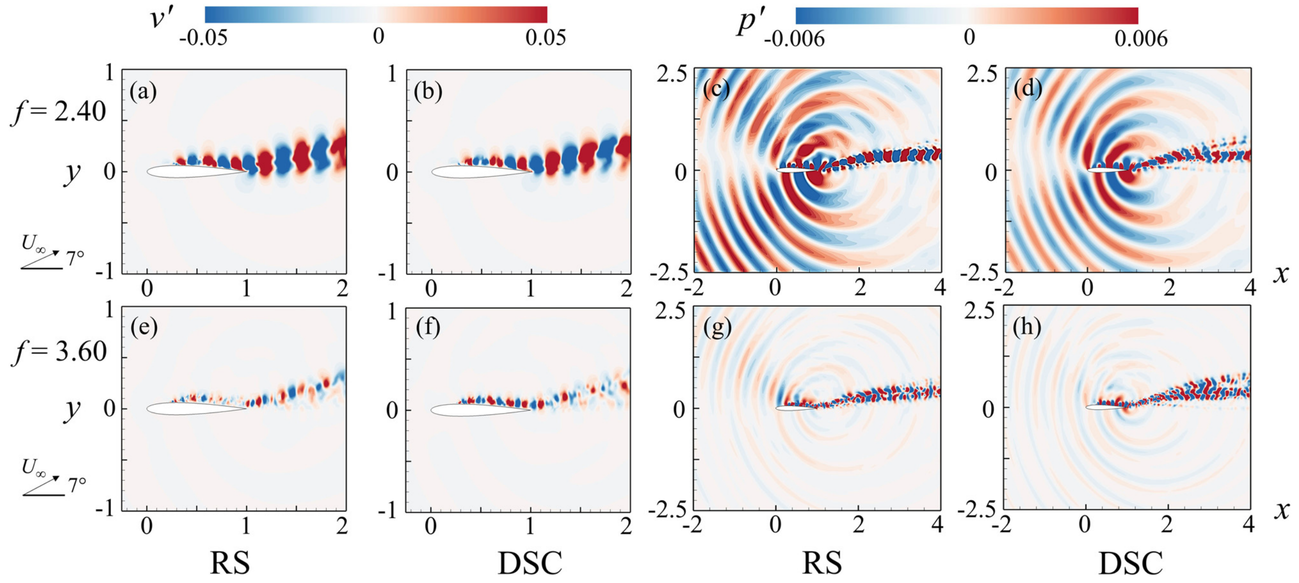

FIG. 19. Filtered FFT distribution of v' [i.e., (a), (b), (e), and (f)] and p' [i.e., (c), (d), (g), and (h)] at $f = 2.40$ (top row) and $f = 3.60$ (bottom row) for RS and DSC airfoils at AoA = 7°.

In order to obtain a deeper understanding of the effects of elastic panels on the flow field features and acoustic generation for DSC airfoil, the fluctuations in the velocity and pressure fields are Fourier transformed in time domain and subsequently filtered for the dominant frequencies $(f_{bl})_0$ corresponding to each AoA and reconstructed in the whole domain. For the filtered FFT analysis, a total of 10 000 snapshots with uniform time interval for a time episode of $t = 10$ is utilized, which correspond to atleast 24 cycles of the lowest frequency of interest. Figures 17–19 illustrate the filtered flow field solutions at the selected dominant frequencies. In these figures, the first two columns are the snapshots of v', and the last two columns are the snapshots of p' for both RS and DSC airfoils at the same time moment.

Figure 17 corresponds to reconstructed filtered v' and p' flow field data at $f = 2.67$ and 2.20 at AoA $= 3°$. It is important to note that for both selected infrequences, the acoustic generation mechanism is found to be similar where the flow instabilities originating from airfoil LSB convect over the trailing edge and scatter as acoustic wave to form an aeroacoustic feedback loop, so no other type of noise generation mechanism exists. At $f = 2.67$, a significant difference in the magnitudes of v' and p' can be observed between RS and DSC airfoils. The low magnitude v' for DSC airfoil at $f = 2.67$ indicates that the vibrating panels are able to suppress the flow instabilities over the airfoil surface effectively and as a result the noise radiation for DSC airfoil appears to be much weaker than RS airfoil. On the other hand, at the shifted dominant frequency $f = 2.20$, the flow instabilities v' and its subsequent acoustic radiation p' are almost similar for both RS and DSC airfoils. This observation shows that the DSC airfoil is able to provide a significant reduction in the flow instabilities at the original dominant frequency of RS airfoil ($f = 2.67$ in this case), and it results in a shift to the frequency of succeeding high magnitude peak (i.e., $f = 2.20$).

Figure 18 illustrates the filtered FFT data of v' and p' flow field data at $f = 3.37$ at AoA $= 5°$ for RS and DSC airfoils, respectively. At AoA $= 5°$, no shift in the dominant frequency is observed in Fig. 13 for DSC airfoil and so the flow field data are plotted for $f = 3.37$ only. The vortex shedding pattern is observed to be similar for both the cases; however, the strength of v' and p' is significantly reduced for

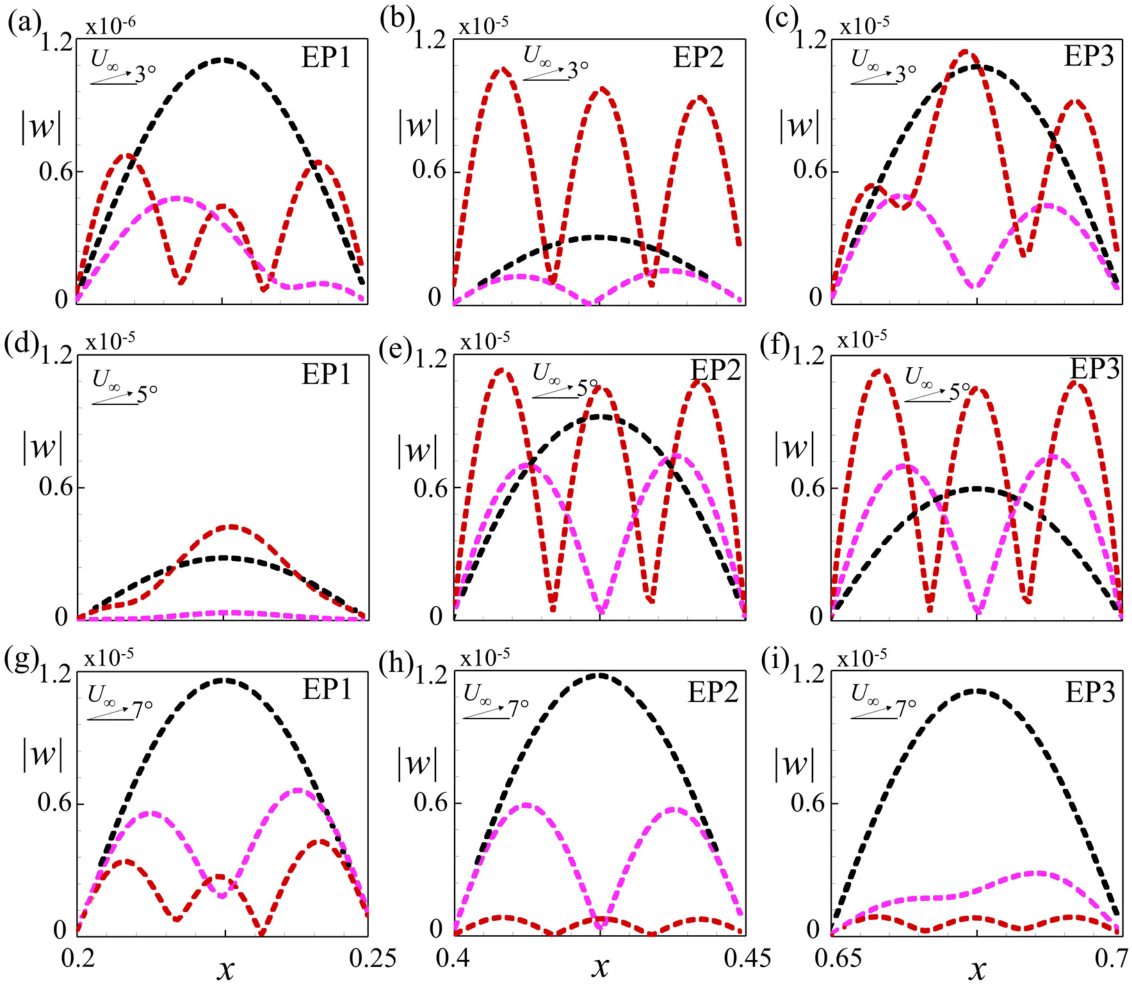

FIG. 20. Comparison of the amplitude of Fourier mode decomposition for first three modes of panels EP1, EP2, and EP3 for DSC airfoil. (a)–(c), AoA $= 3°$; (d)–(f), AoA $= 5°$; (g)–(i), AoA $= 7°$.

DSC airfoil. A maximum noise reduction is achieved at this AoA by DSC airfoil as observed in Figure 16.

Figure 19 corresponds to reconstructed filtered v' and p' flow field data at $f = 2.40$ and 3.60 at AoA $= 7°$. At $f = 2.40$, only a slight reduction in the magnitudes of v' and p' can be observed for DSC airfoil. As a result, the noise reduction by DSC airfoil at this AoA is observed to be much lower than other AoAs. At the shifted dominant frequency of $f = 3.60$, the flow instabilities v' and its subsequent acoustic radiation p' are almost similar for both RS and DSC airfoils, which is analogous to the observed phenomenon of frequency shifting at AoA $= 3°$.

3. Panels inter-dynamical structural analysis

From the acoustic and aerodynamic flow analyses in the preceding sections, it is well ascertained that the DSC airfoil is able to provide considerable airfoil tonal noise reduction at all AoAs. However, it is essential to understand the role of panel structural dynamics and its impact on noise reduction capabilities of DSC airfoil at different AoAs. The vibratory response of the panels under the fluid loading is initially examined in both spatial and temporal domains to identify the key dynamical features. In this regard, the Fourier mode decomposition (FMD) analysis is utilized to extract the vibration modes of interest and analyze the panel displacement at these modes.[64] For FMD analysis, the panel displacement data w are arranged in a time-space matrix, and FFT is employed to transform it into frequency-space domain. The dominant vibration modes of each elastic panel $f_{EP_{1,2,3}}$ (corresponding to first, second, and third mode, respectively) are extracted by plotting the Fourier amplitude of w along each panel location.

Figures 20(a)–20(c) show the extracted modal shapes for all the panels in DSC airfoil at AoA $= 3°$. As discussed in preceding sections, all the panels are designed to vibrate in their respective third modes. The FMD analysis shows the dominance of first mode for panel EP1 with a magnitude of one order lower than other panels. On the other hand, the panel EP2 vibrates in the third dominant mode and panel EP3 vibrates in both the first and third dominant modes. It is important to note that the design of the panel EP3 is based on the flow characteristics of the airfoil at AoA $= 3°$. The fact that the panel EP3 vibrating in its third dominant mode is favorable in inhibiting the boundary layer instabilities over the airfoil suction surface. Hence, a considerable noise reduction is observed for DSC airfoil at AoA $= 3°$ as observed in Fig. 16.

Figures 20(d)–20(f) show the extracted modal shapes for all the panels in DSC airfoil at AoA $= 5°$. At this AoA, the panel EP1 vibrates in third mode with much weaker magnitude than other panels. On the other hand, panels EP2 and EP3 vibrate in third dominant modes with much higher magnitudes. Since all the panels tend to vibrate in their desired third mode shapes, the noise reduction by DSC airfoil at AoA $= 5°$ is observed to be much higher than other AoAs, which signifies the importance of panel vibrational behavior in noise reduction capability of DSC airfoil.

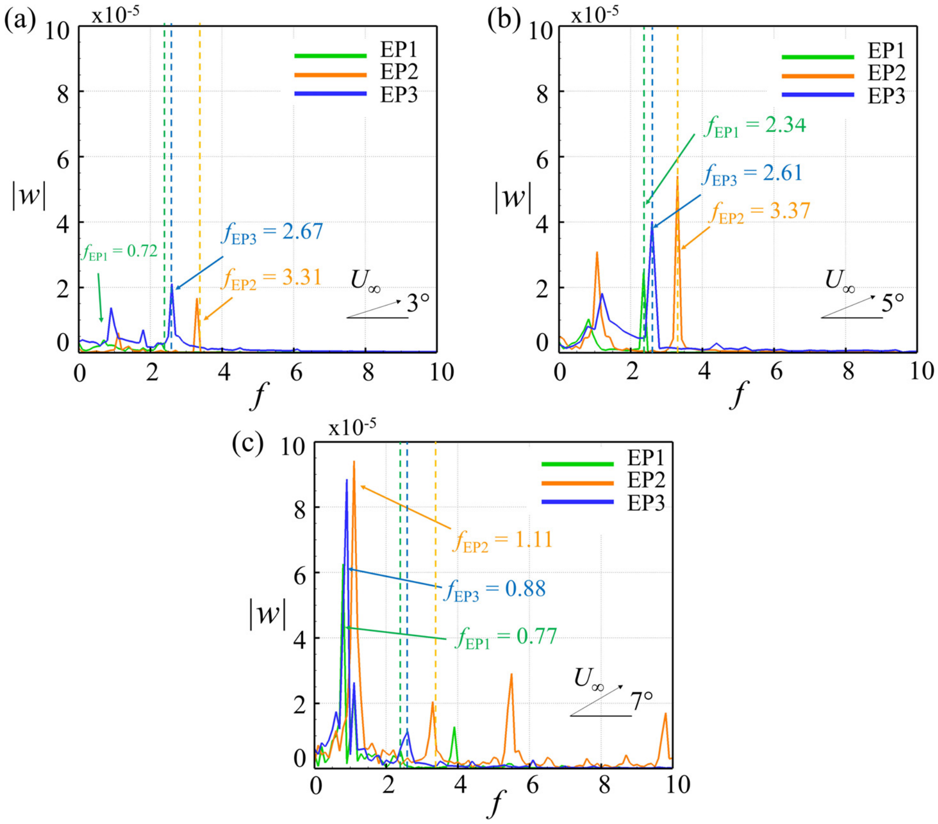

FIG. 21. FFT spectra of panels displacement for DSC airfoil. (a) AoA $= 3°$; (b) AoA $= 5°$; and (c) AoA $= 7°$. The vertical dashed lines indicate the panels' resonance frequencies.

Figures 20(g)–20(i) show the extracted modal shapes for all the panels in DSC airfoil at AoA = 7°. In contrast to AoA = 5°, all the panels tend to vibrate in their first dominant mode. As a result, the noise reduction effectiveness of DSC airfoil at AoA = 7° is slightly degraded as compared with other AoAs. Nevertheless, the designed panels for DSC airfoil are still able to provide some noise reduction even when the desired mode shape is not attained.

Figures 21(a)–21(c) show the FFT spectrum of w for all the panels of DSC airfoil at each AoA. The vertical dashed lines indicate the desired resonance frequency for each panel according to its color code. At AoA = 3°, the panels EP2 and EP3 vibrate at their resonance frequencies in the third mode at $f = 3.37$ and 2.67, respectively; whereas, the panel EP1 vibrates in its first mode at $f = 0.72$. It indicates that the panel vibrations at other than their desired resonance frequency (EP1 in this case) may affect the noise reduction effectiveness of the airfoil to some extent as discussed in FMD analysis. At AoA = 5°, all the panels EP1, EP2, and EP3 vibrate at their resonance frequencies in the third mode at $f = 2.34$, 3.37, and 2.67, respectively. Since all the panels maintain their desired mode shape and resonance condition, the noise reduction effectiveness of the DSC airfoil is observed to be much higher than other AoAs. Furthermore, no change in the spectral content of the flow is observed at this AoA (Fig. 13). At AoA = 7°, all the panels are found to deviate from their desired resonance frequencies. As a result, the overall noise reduction potential of DSC airfoil is also reduced at AoA = 7° as observed in Fig. 16.

The fluid–structure interactions of the panels on DSC airfoil and their associated vibration responses are investigated by analyzing the pressure fluctuations p' within one complete hydrodynamic cycle counting from the moment of maximum lift for each AoA together with the corresponding panel displacement. Figure 22 shows the fluid-structure interactions of DSC airfoil at AoA = 3°. The region corresponding to panel EP3 is subjected to prominent high and low pressure fluctuations due to the growth of flow instabilities as observed in Fig. 12(b). The panel EP3 is observed to vibrate in third mode shape throughout the cycle. The panel EP2 shows some variation in mode shape between second and third modes at different instances. On the

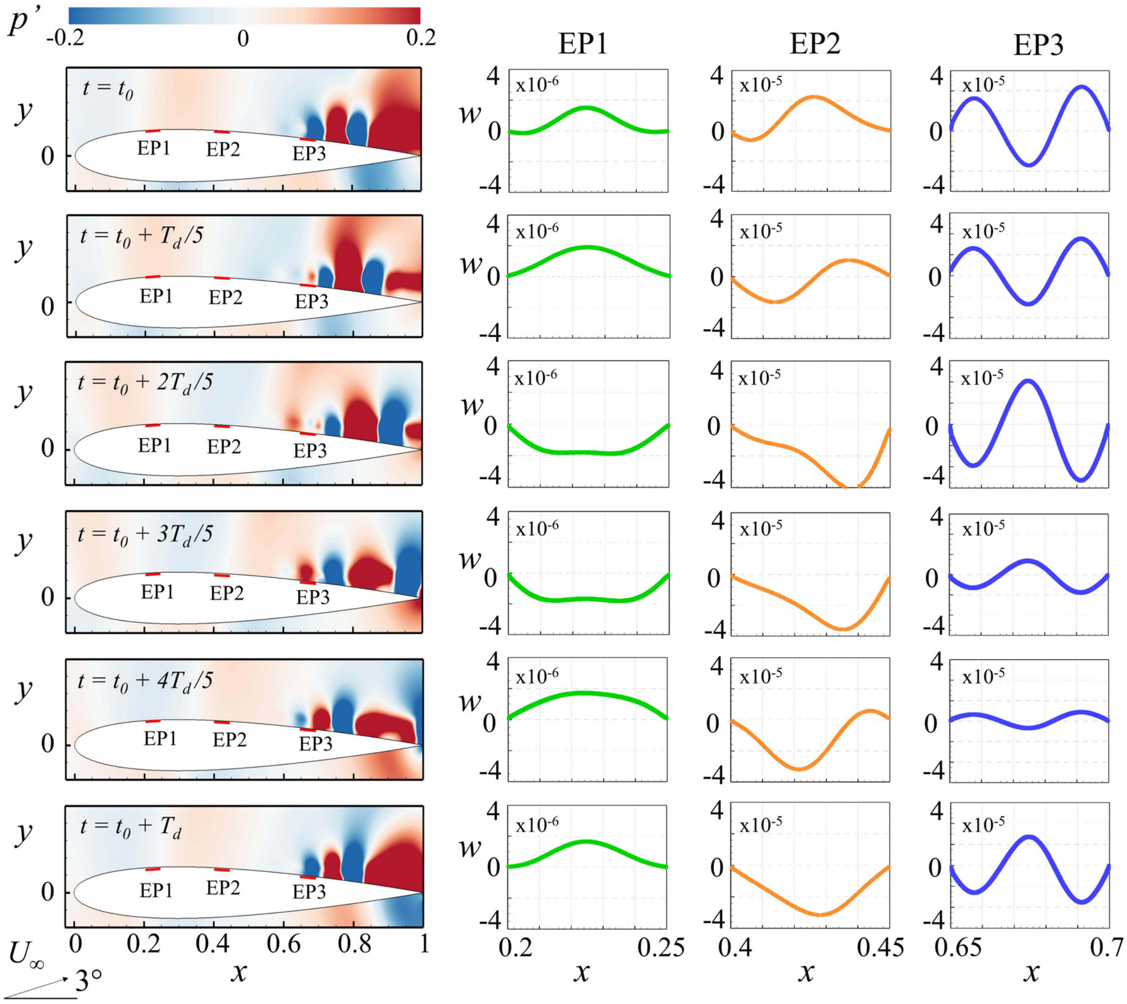

FIG. 22. Snapshots of the p' distribution over the panels and panel displacements for DSC airfoil within one period $T_d = 1/(f_{bl})_0$ at AoA = 3°.

other hand, the panel EP1 maintains first mode throughout the cycle with much lower amplitude than other panels.

Figure 23 shows the fluid-structure interactions of DSC airfoil at AoA $= 5°$. The regions corresponding to panels EP2 and EP3 are subjected to prominent high and low pressure fluctuations as the growth of flow instabilities shifts upstream at this AoA. All the panels maintain a well-defined third mode shape at all instances throughout the cycle, which agrees with the panels FFT spectrum (Fig. 21).

Figure 24 shows the fluid-structure interactions of DSC airfoil at AoA $= 7°$. All the panels are subjected to prominent high and low pressure fluctuations at AoA $= 7°$ as the separation bubble shifts further upstream toward leading edge of the airfoil. The panel displacements of EP1 and EP2 are non-uniform throughout the cycle whereas the panel EP3 maintains first mode shape at all instances.

The impact of panels vibrational response on the flow dynamics and its consequence to airfoil acoustics is further investigated by coherence analysis. The analysis is performed between the p' signal at a location $(r, \theta) = (3, 135°)$ [marked as location A in Fig. 1(c)] and v' signal within the boundary layer along a streamline at an average offset of $\Delta y = 10^{-5}$ over the suction surface, which is divided into 2000 segments. The magnitude-squared coherence $\gamma_{12}^2(f)$ between the p' and v' signals[65] is calculated by

$$\gamma_{12}^2(f) = \frac{|P_{12}(f)|^2}{P_{11}(f)P_{22}(f)}, \tag{7}$$

where $P_{11}(f)$ and $P_{22}(f)$ are the power spectral densities of v' and p' signals, respectively, and $P_{12}(f)$ is the cross power spectral density of both the signals.

Figures 25(a)–25(f) illustrate the coherence spectra for RS and DSC airfoils at all AoAs. The horizontal dashed dot lines indicate the $(f_{bl})_0$ at each AoA whereas the vertical dashed lines indicate the coverage of panels for DSC airfoil. At AoA $= 3°$, a strong coherence is observed between the acoustic waves and airfoil flow along the chord for RS airfoil at $(f_{bl})_0 = 2.67$. The coherency is significantly reduced at $(f_{bl})_0 = 2.67$ for DSC airfoil, which indicates that the panels vibrations

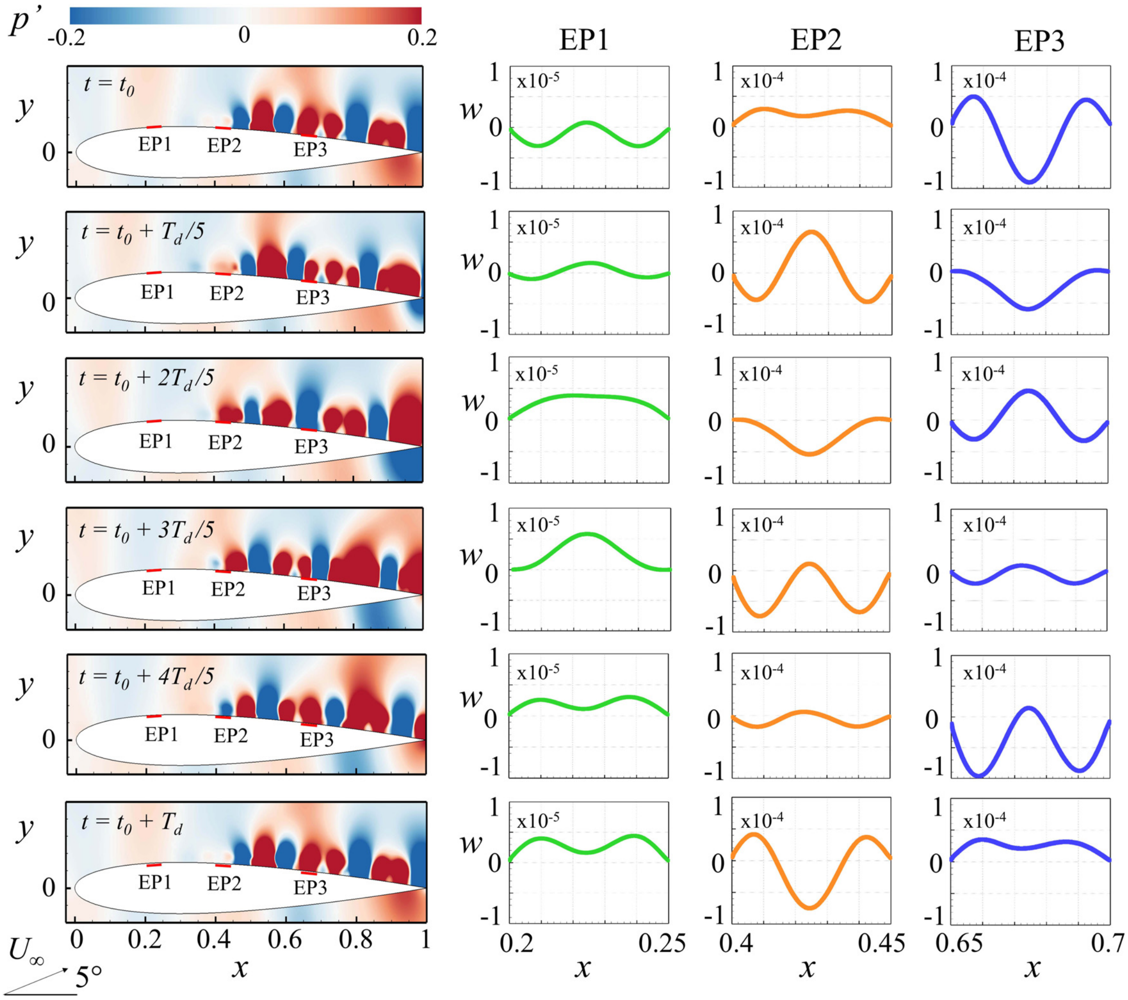

FIG. 23. Snapshots of the p' distribution over the panels and panel displacements for DSC airfoil within one period $T_d = 1/(f_{bl})_0$ at AoA $= 5°$.

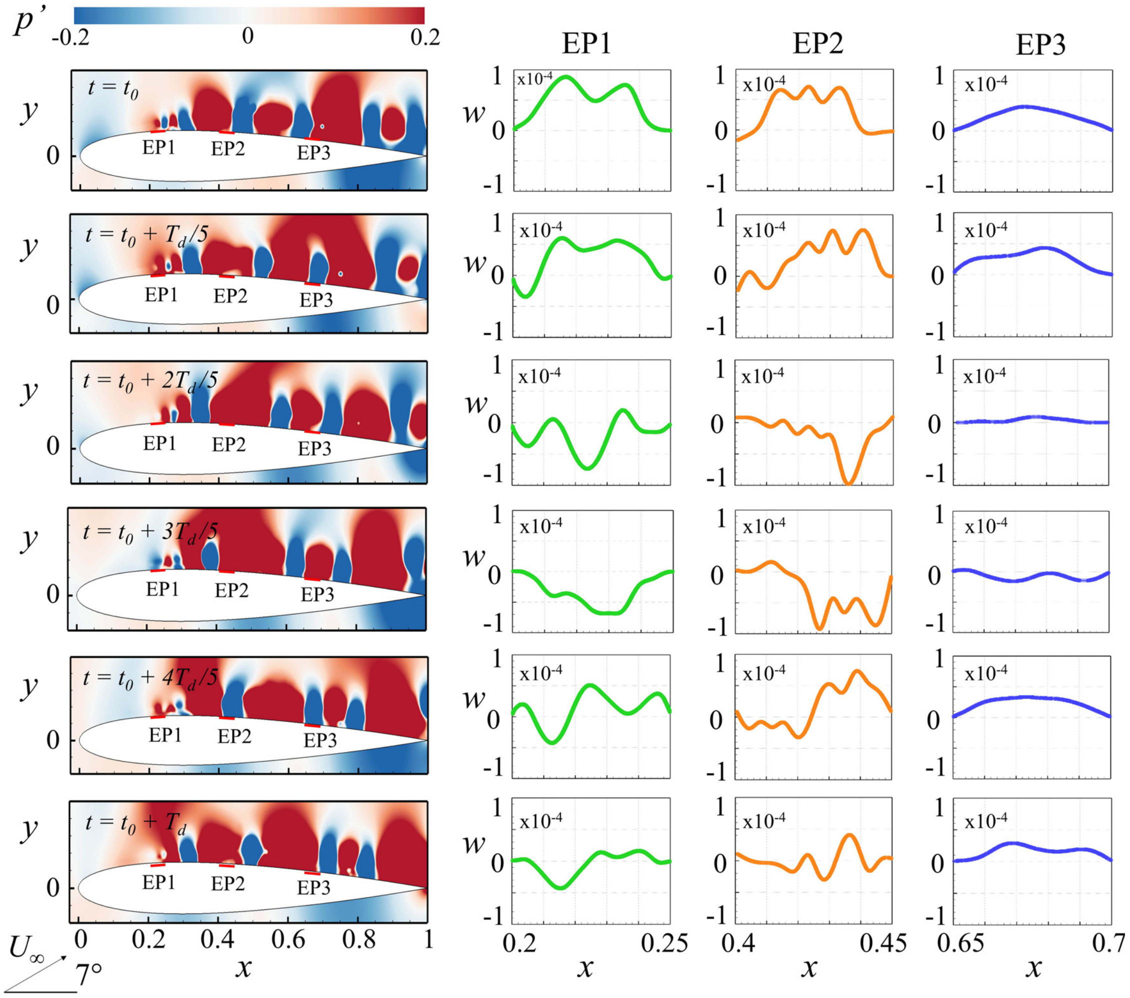

FIG. 24. Snapshots of the p' distribution over the panels and panel displacements for DSC airfoil within one period $T_d = 1/(f_{bl})_0$ at AoA $= 7°$.

have remarkably influenced the acoustic generation by the airfoil. A slight increase in $\gamma_{12}^2(f)$ is observed within $0.05 < x < 0.35$ for DSC airfoil at $f = 2.20$; however, its magnitude is still much less than that of RS airfoil at the $(f_{bl})_0 = 2.67$ at the same locations. At AoA $= 5°$, the significant reduction in $\gamma_{12}^2(f)$ at $(f_{bl})_0 = 3.37$ is observed for DSC airfoil from $0.2 < x < 1$. Interestingly, the coherency at higher harmonics is also significantly reduced for DSC airfoil at AoA $= 5°$. At AoA $= 7°$, the reduction in $\gamma_{12}^2(f)$ at $(f_{bl})_0 = 2.40$ is observed to be less pronounced as compared with other AoAs. Hence, the noise reduction effectiveness of DSC airfoil is also observed to be lower at this AoA.

Based on the comprehensive aeroacoustic and structural analyses, it is evident that the complex fluid–structure interactions occurring over the panels for DSC airfoil has a great influence on the airfoil acoustics and overall airfoil flow field characteristics. The extent of noise reduction with respect to AoA is observed to be non-uniform for DSC airfoil. Coincidence with panel vibrational mode shape and achievement of panel resonance are found to be the major contributing factors in the noise reduction effectiveness of DSC airfoil. In the present study, these factors prevail fully with the flow at AoA $= 5°$ where the vibrations of all panels tend to resonate in their desired third modes and maximum noise reduction is achieved. At lower AoA, one of the panels is found to vibrate in the first mode, which limits the noise reduction effectiveness of DSC airfoil. In contrast, at higher AoA, all the panels are vibrating far away from their desired mode shapes which severely reduces the noise reduction potential of DSC airfoil. Nevertheless, a considerable average noise reduction is observed over a complete range of AoA for DSC airfoil, which can be utilized for different low *Re* aerodynamic devices operating at various loading conditions.

VI. CONCLUSIONS

A novel concept of utilizing distributed surface compliance for reduction of tonal noise of airfoil has been studied numerically in detail and evaluated with a uniform flow at Reynolds number $Re = 5 \times 10^4$ and Mach number $M = 0.4$ past a NACA 0012 airfoil.

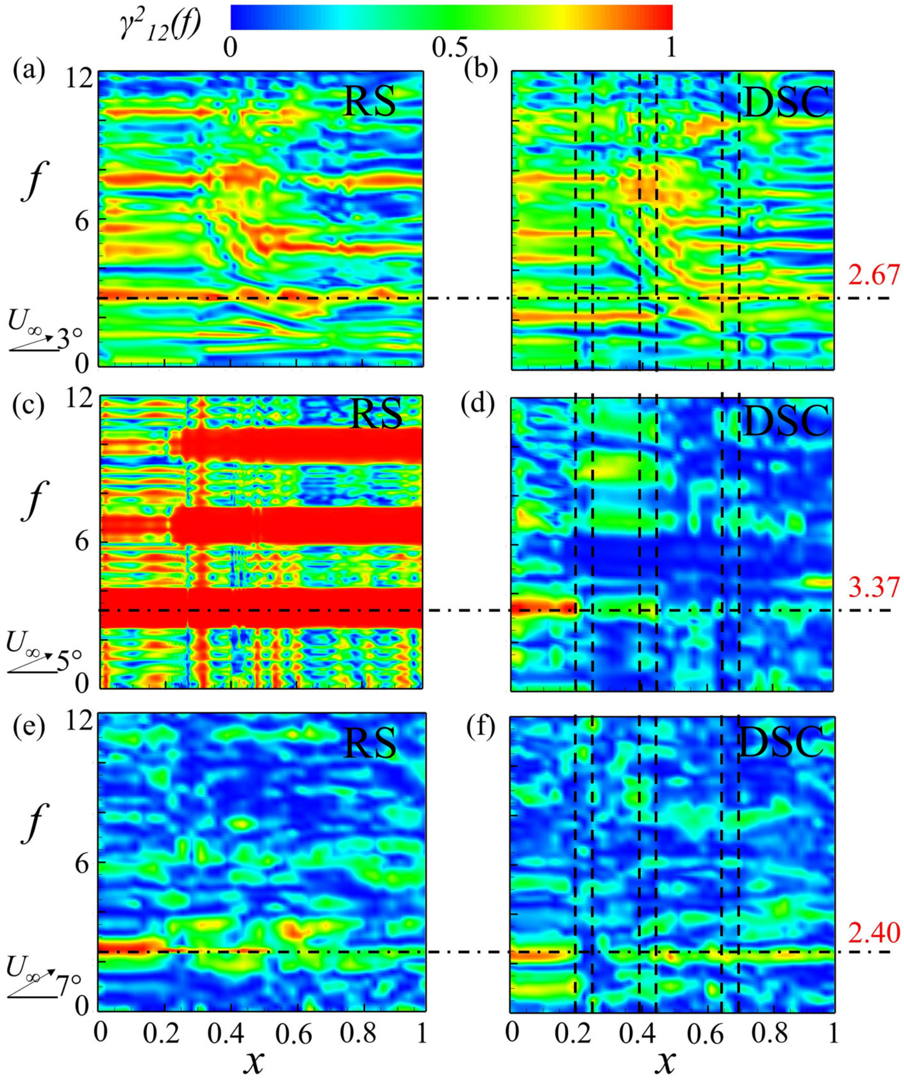

FIG. 25. Spectra of magnitude-squared coherence $\gamma^2_{12}(f)$ between the acoustic signal at $(r, \theta) = (3, 135^\circ)$ and velocity signals along airfoil chord. (a) and (b), AoA $= 3^\circ$. (c) and (d), AoA $= 5^\circ$. (e) and (f), AoA $= 7^\circ$. The horizontal dashed-dot lines indicate the $(f_{bl})_0$ at each AoA, and the vertical dashed lines indicate the coverage of panels for DSC airfoil.

The distributed surface compliance is facilitated by mounting short elastic panels at appropriate locations on airfoil suction surface. The salient feature of the proposed concept rests with the fact that the modified airfoil (i.e., DSC airfoil) is able to give consistent tonal noise reduction at various loading conditions under different angles of attack AoAs without any sacrifice in its aerodynamics. The design framework of the DSC airfoil is based on the flow characteristics of the rigid surface (RS) airfoil. Initially, different single elastic panel (SEP) configurations are designed for the airfoil AoAs of interest, and their effectiveness in tonal noise reduction is ascertained using perturbation evolution method (PEM) for quick assessment. The analysis reveals that a significant reduction in tonal noise can be achieved at each AoA by utilizing the structural resonance of elastic panel; however, the effectiveness of SEP in noise reduction is significantly reduced at their off-design AoAs. Hence, the distributed surface compliance (DSC) airfoil can be carefully designed to achieve tonal noise reduction over a complete operational range of AoA.

A comprehensive aeroacoustic and fluid-structure interaction analyses are performed using DAS and compared with RS airfoil. The results of the comprehensive acoustic analyses, using high-fidelity direct aeroacoustic simulation, reveal that the DSC airfoil could effectively provide a significant noise reduction up to 7 dB over the complete range of AoA without any adverse effect on airfoil aerodynamics. Spectral analysis of the DSC airfoil flow indicates that a significant reduction in the strength of the flow instabilities is observed for AoA $= 3^\circ$ and 5° whereas a mild reduction is observed at higher AoA. This aspect is further uncovered with Fourier mode decomposition analysis of dynamic behaviors of the flow-induced vibrating panels. The analysis reveals that at lower AoA, the designed panels vibrate in their desired mode shape in resonance condition, which results in the suppression of flow instabilities over the airfoil suction surface and eventually leads to higher tonal noise reduction, whereas, at higher AoA, the panels vibrate in their first mode, which results in a relatively low noise reduction. Nevertheless, considerable noise reduction is still achieved by DSC airfoil at all loading conditions, which substantiates its applicability in different low Reynolds number aerodynamic devices.

ACKNOWLEDGMENTS

The authors gratefully acknowledge the support from a research donation from the Philip K. H. Wong Foundation under Grant No. 5-ZH1X. I.A. and M.R.N. gratefully acknowledge the support with research studentship tenable at Department of Mechanical Engineering, The Hong Kong Polytechnic University (PolyU). G.C.Y.L. and R.C.K.L. are grateful to the support from the Research Grants Council of the Government of Hong Kong Special Administrative Region under Grant Nos. 15208520 and A-PolyU 503/15. The provision of computer times by University Research Facility in Big Data Analytics (UBDA) at PolyU is much appreciated.

AUTHOR DECLARATIONS

Conflict of Interest

The authors have no conflicts to disclose.

DATA AVAILABILITY

The data that support the findings of this study are available from the corresponding author upon reasonable request.

REFERENCES

[1] T. F. Brooks, D. S. Pope, and M. A. Marcolini, "Airfoil self-noise and prediction," Report No. NAS 1.61:1218 (NASA, 1989).

[2] H. Arbey and J. Bataille, "Noise generated by airfoil profiles placed in a uniform laminar flow," J. Fluid Mech. **134**, 33–47 (1983).

[3] M. Alam and N. D. Sandham, "Direct numerical simulation of short laminar separation bubbles with turbulent reattachment," J. Fluid Mech. **410**, 1–28 (2000).

[4] G. Desquesnes, M. Terracol, and P. Sagaut, "Numerical investigation of the tone noise mechanism over laminar airfoils," J. Fluid Mech. **591**, 155–182 (2007).

[5] S. Pröbsting and S. Yarusevych, "Laminar separation bubble development on an airfoil emitting tonal noise," J. Fluid Mech. **780**, 167–191 (2015).

[6] R. W. Paterson, P. G. Vogt, M. R. Fink, and C. L. Munch, "Vortex noise of isolated airfoils," J. Aircraft **10**, 296–302 (1973).

[7] C. K. W. Tam, "Discrete tones of isolated airfoils," J. Acoust. Soc. Am. **55**, 1173–1177 (1974).

[8] E. C. Nash, M. V. Lowson, and A. McAlpine, "Boundary-layer instability noise on aerofoils," J. Fluid Mech. **382**, 27–61 (1999).

[9] A. McAlpine, E. C. Nash, and M. V. Lowson, "On the generation of discrete frequency tones by the flow around an aerofoil," J. Sound Vib. **222**, 753–779 (1999).

[10] M. Fosas de Pando, P. J. Schmid, and D. Sipp, "A global analysis of tonal noise in flows around aerofoils," J. Fluid Mech. **754**, 5–38 (2014).

[11] E. Arcondoulis, C. J. Doolan, A. C. Zander, and L. A. Brooks, "An experimental investigation of airfoil tonal noise caused by an acoustic feedback loop," in *Proceedings of Acoustics* (Victor Harbor, Australia, 2013), pp. 42–49.

[12] S. Pröbsting, J. Serpieri, and F. Scarano, "Experimental investigation of aerofoil tonal noise generation," J. Fluid Mech. **747**, 656–687 (2014).

[13] Y. Yang, S. Pröbsting, Y. Liu, H. Zhang, C. Li, and Y. Li, "Effect of dual vortex shedding on airfoil tonal noise generation," Phys. Fluids **33**, 075102 (2021).

[14] L. E. Jones, R. D. Sandberg, and N. D. Sandham, "Stability and receptivity characteristics of a laminar separation bubble on an aerofoil," J. Fluid Mech. **648**, 257–296 (2010).

[15] S. Pröbsting and S. Yarusevych, "Airfoil flow receptivity to simulated tonal noise emissions," Phys. Fluids **33**, 044106 (2021).

[16] T. P. Chong, A. Vathylakis, P. F. Joseph, and M. Gruber, "Self-noise produced by an airfoil with nonflat plate trailing-edge serrations," AIAA J. **51**, 2665–2677 (2013).

[17] J. Wang, C. Zhang, Z. Wu, J. Wharton, and L. Ren, "Numerical study on reduction of aerodynamic noise around an airfoil with biomimetic structures," J. Sound Vib. **394**, 46–58 (2017).

[18] S. S. Vemuri, X. Liu, B. Zang, and M. Azarpeyvand, "On the use of leading-edge serrations for noise control in a tandem airfoil configuration," Phys. Fluids **32**, 077102 (2020).

[19] A. Celik, J. L. Bowen, and M. Azarpeyvand, "Effect of trailing-edge bevel on the aeroacoustics of a flat-plate," Phys. Fluids **32**, 105116 (2020).

[20] A. Celik, Y. Mayer, and M. Azarpeyvand, "On the aeroacoustic characterization of a robust trailing-edge serration," Phys. Fluids **33**, 075120 (2021).

[21] C. Teruna, F. Avallone, D. Ragni, and D. Casalino, "On the noise reduction of a porous trailing edge applied to an airfoil at lifting condition," Phys. Fluids **33**, 055132 (2021).

[22] Y. Shi and W. Kollmann, "Improved delayed detached eddy simulation of a porous wavy trailing edge," Phys. Fluids **33**, 055128 (2021).

[23] T. P. Chong and P. F. Joseph, "An experimental study of airfoil instability tonal noise with trailing edge serrations," J. Sound Vib. **332**, 6335–6358 (2013).

[24] P. W. Bearman and J. C. Owen, "Reduction of bluff-body drag and suppression of vortex shedding by the introduction of wavy separation lines," J. Fluids Struct. **12**, 123–130 (1998).

[25] D. Misklosovic and M. Murray, "Leading edge tubercles, delay stall on humpback whale flipper," Phys. Fluids **16**, L39–L42 (2004).

[26] F. Fish and G. Lauder, "Passive and active flow control by swimming fishes and mammals," Annu. Rev. Fluid Mech. **38**, 193–224 (2006).

[27] K. L. Hansen, N. Rostamzadeh, R. M. Kelso, and B. B. Dally, "Evolution of the streamwise vortices generated between leading edge tubercles," J. Fluid Mech. **788**, 730–766 (2016).

[28] D. J. Moreau and C. J. Doolan, "The generation of tonal noise from sawtooth trailing-edge serrations at low Reynolds numbers," Aeronaut. J. **120**, 971 (2016).

[29] C. Jiang, J. R. Fischer, D. J. Moreau, and C. J. Doolan, "Experimental investigation of novel porous-serrated treatments on airfoil trailing edge noise reduction," AIAA Paper No. AIAA 2019-2435, 2019.

[30] L. Kamps, C. Brücker, T. F. Geyer, and E. Sarradj, "Airfoil self noise reduction at low Reynolds numbers using a passive flexible trailing edge," AIAA Paper No. AIAA 2017-3496, 2017.

[31] E. Talboys and C. Brücker, "Upstream shear-layer stabilisation via self-oscillating trailing edge flaplets," Exp. Fluids **59**, 145 (2018).

[32] M. S. Genç, A. ikel, and K. Koca, "Effect of partial flexibility over both upper and lower surfaces to flow over wind turbine airfoil," Energy Convers. Manage. **219**, 113042 (2020).

[33] P. Zhou, Q. Liu, S. Zhong, Y. Fang, and X. Zhang, "A study of the effect of serration shape and flexibility on trailing edge noise," Phys. Fluids **32**, 127114 (2020).

[34] E. Talboys, T. F. Geyer, and C. Brücker, "An aeroacoustic investigation into the effect of self-oscillating trailing edge flaplets," J. Fluids Struct. **91**, 102598–102511 (2019).

[35] S. C. Schlanderer and R. D. Sandberg, "Direct numerical simulation of a compliant trailing-edge flow," AIAA Paper No. 2013–2013, 2013.

[36] I. Arif, G. C. Y. Lam, R. C. K. Leung, and D. Wu, "Leveraging surface aeroacoustic-structural interaction for airfoil tonal noise reduction," AIAA Paper No. AIAA 2019-2758, 2019.

[37] M. V. Lowson, S. P. Fiddes, and E. C. Nash, "Laminar boundary layer aeroacoustic instabilities," AIAA Paper No. AIAA 94-0358, 1994.

[38] R. D. Sandberg, L. E. Jones, N. D. Sandham, and P. F. Joseph, "Direct numerical simulations of noise generated by airfoil trailing edges," AIAA Paper No. AIAA 2007-3469, 2007.

[39] L. E. Jones, R. D. Sandberg, and N. D. Sandham, "Direct numerical simulations of forced and unforced separation bubbles on an airfoil at incidence," J. Fluid Mech. **602**, 175–207 (2008).

[40] S. Pröbsting, F. Scarano, and S. C. Morris, "Regimes of tonal noise on an airfoil at moderate Reynolds number," J. Fluid Mech. **780**, 407–438 (2015).

[41] R. Wang and Z. Xiao, "Transition effects on flow characteristics around a static two-dimensional airfoil," Phys. Fluids **32**, 035113 (2020).

[42] J. Tank, B. Klose, G. Jacobs, and G. Spedding, “Flow transitions on a cambered airfoil at moderate Reynolds number,” Phys. Fluids **33**, 093105 (2021).

[43] I. Arif, D. Wu, G. C. Y. Lam, and R. C. K. Leung, “Exploring airfoil tonal noise reduction with elastic panel using perturbation evolution method,” AIAA J. **58**, 4958–4968 (2020).

[44] G. C. Y. Lam, R. C. K. Leung, K. H. Seid, and S. K. Tang, “Validation of CE/SE scheme in low Mach number direct aeroacoustic simulation,” Int. J. Nonlinear Sci. Numer. Simul. **15**, 157–169 (2014).

[45] G. C. Y. Lam, R. C. K. Leung, and S. K. Tang, “Aeroacoustics of duct junction flows merging at different angles,” J. Sound Vib. **333**, 4187–4202 (2014).

[46] G. C. Y. Lam and R. C. K. Leung, “Aeroacoustics of NACA 0018 airfoil with a cavity,” AIAA J. **56**, 4775–4786 (2018).

[47] I. Arif, G. C. Y. Lam, D. Wu, and R. C. K. Leung, “Passive airfoil tonal noise reduction by localized flow-induced vibration of an elastic panel,” Aerosp. Sci. Technol. **107**, 106319 (2020).

[48] E. H. Dowell, *Aeroelasticity of Plates and Shells* (Noordhoff International Publishing, Leyden, 1975).

[49] H. K. H. Fan, R. C. K. Leung, G. C. Y. Lam, Y. Aurégan, and X. Dai, “Numerical coupling strategy for resolving in-duct elastic panel aeroacoustic/structural interaction,” AIAA J. **56**, 5033–5040 (2018).

[50] H. K. H. Fan, R. C. K. Leung, and G. C. Y. Lam, “Numerical analysis of aeroacoustic-structural interaction of a flexible panel in uniform duct flow,” J. Acoust. Soc. Am. **137**, 3115–3126 (2015).

[51] J. Aguilar-Cabello, P. Gutierrez-Castillo, L. Parras, C. del Pino, and E. Sanmiguel-Rojas, “On the onset of negative lift in a symmetric airfoil at very small angles of attack,” Phys. Fluids **32**, 055107 (2020).

[52] L. E. Jones and R. D. Sandberg, “Numerical analysis of tonal airfoil self-noise and acoustic feedback-loops,” J. Sound Vib. **330**, 6137–6152 (2011).

[53] P. Balakumar, “Direct numerical simulation of flows over an NACA-0012 airfoil at low and moderate Reynolds numbers,” AIAA Paper No. AIAA 2017-3978, 2017.

[54] M. J. Lighthill, “On sound generated aerodynamically II. Turbulence as a source of sound,” Proc. R. Soc. London, Ser. A **222**, 1–32 (1954).

[55] F. Williams and L. H. Hall, “Aerodynamic sound generation by turbulent flow in the vicinity of a scattering half plane,” J. Fluid Mech. **40**, 657–670 (1970).

[56] D. G. Crighton and F. G. Leppington, “On the scattering of aerodynamic noise,” J. Fluid Mech. **46**, 577–597 (1971).

[57] T. R. Ricciardi, W. Arias-Ramirez, and W. R. Wolf, “On secondary tones arising in trailing-edge noise at moderate Reynolds numbers,” Eur. J. Mech.-B/Fluids **79**, 54–66 (2020).

[58] T. Ricciardi, W. Wolf, and K. Taira, “Laminar-turbulent transition and intermittency effects on secondary tones from a NACA 0012 airfoil,” AIAA Paper No. AIAA 2021-2295, 2021.

[59] F. J. Fahy and P. Gardonio, *Sound and Structural Vibration: Radiation, Transmission and Response*, 2nd ed. (Elsevier, 2007).

[60] R. D. Blevins, *Formulas for Natural Frequency and Mode Shape* (Van Nostrand Reinhold Company, New York, 1979), pp. 226–227.

[61] P. Chaitanya, P. F. Joseph, S. Narayanan, C. Vanderwel, J. Turner, J. Kim, and B. Ganapathisubramani, “Performance and mechanism of sinusoidal leading edge serrations for the reduction of turbulence–aerofoil interaction noise,” J. Fluid Mech. **818**, 435–464 (2017).

[62] F. Avallone, W. C. P. Van Der Velden, D. Ragni, and D. Casalino, “Noise reduction mechanisms of sawtooth and combed-sawtooth trailing-edge serrations,” J. Fluid Mech. **848**, 560–591 (2018).

[63] S. Serrano-Galiano, N. D. Sandham, and R. D. Sandberg, “Fluid–structure coupling mechanism and its aerodynamic effect on membrane aerofoils,” J. Fluid Mech. **848**, 1127–1156 (2018).

[64] G. Li, B. C. Khoo, and R. K. Jaiman, “Computational aeroelasticity of flexible membrane wings at moderate Reynolds numbers,” AIAA Paper No. AIAA 2020-2036, 2020.

[65] P. Stoica and R. Moses, *Spectral Analysis of Signals*, 1st ed. (Pearson Prentice Hall, Upper Saddle River, NJ, 2005).